Deep Convective Organization, Moisture Vertical Structure, and Convective Transition Using Deep-Inflow Mixing

KATHLEEN A. SCHIRO[a] AND J. DAVID NEELIN

Department of Atmospheric and Oceanic Sciences, University of California, Los Angeles, Los Angeles, California

(Manuscript received 24 April 2018, in final form 19 December 2018)

ABSTRACT

It is an open question whether an integrated measure of buoyancy can yield a strong relation to precipitation across tropical land and ocean, across the seasonal and diurnal cycles, and for varying degrees of convective organization. Building on previous work, entraining plume buoyancy calculations reveal that differences in convective onset as a function of column water vapor (CWV) over land and ocean, as well as seasonally and diurnally over land, are largely due to variability in the contribution of lower-tropospheric humidity to the total column moisture. Over land, the relationship between deep convection and lower-free-tropospheric moisture is robust across all seasons and times of day, whereas the relation to boundary layer moisture is robust for the daytime only. Using S-band radar, these transition statistics are examined separately for mesoscale and smaller-scale convection. The probability of observing mesoscale convective systems sharply increases as a function of lower-free-tropospheric humidity. The consistency of this with buoyancy-based parameterization is examined for several mixing formulations. Mixing corresponding to deep inflow of environmental air into a plume that grows with height, which incorporates nearly equal weighting of boundary layer and free-tropospheric air, yields buoyancies consistent with the observed onset of deep convection across the seasonal and diurnal cycles in the Amazon. Furthermore, it provides relationships that are as strong or stronger for mesoscale-organized convection as for smaller-scale convection.

1. Introduction

Convection is a key process in the hydrologic and energy cycles through the vertical transport of heat, moisture, and momentum, and thus largely affects the global energy balance. Representing convection at the right time and place is crucial to the realistic simulation of atmospheric variability. However, the representation of convection remains a large source of uncertainty, bias, and error in current-generation numerical weather prediction and climate models (Knight et al. 2007; Sanderson et al. 2008). Errors in simulated precipitation fields often indicate deficiencies in the representation of these physical processes in models. Improving the representation of deep convection thus depends on knowledge of leading-order controls and further requires the development of robust observational constraints from statistical relations that describe these controls.

The uncertainty linked to deep convection lies primarily within a model's representation of complicated interactions across scales and the onset of deep convection. Since most of the present-day general circulation models (GCMs) cannot explicitly resolve the small-scale physics of convection, the ensemble effect of convection is represented through parameterization. Differences among the different convective parameterizations lie substantially in the identification of the source layer of convection and how convective instability is defined and released (Suhas and Zhang 2014). Observational constraints on these processes would provide much-needed insight into the physical basis of these parameterizations.

Numerical experiments of the diurnal cycle of precipitation reveal that the parameterization is the main source of error (Betts and Jakob 2002; Bechtold et al. 2004; Guichard et al. 2004; Knievel et al. 2004; Xie et al. 2004; Lee et al. 2007), and sensitivity experiments show

Supplemental information related to this paper is available at the Journals Online website: https://doi.org/10.1175/JAS-D-18-0122.s1.

[a] Current affiliation: Jet Propulsion Laboratory, California Institute of Technology, Pasadena, California.

Corresponding author: Kathleen A. Schiro, kschiro@atmos.ucla.edu

DOI: 10.1175/JAS-D-18-0122.1

that certain parameterizations work better for some geographic regions or environments than others, indicating the limitations of parameterizations in considering a range of dynamical and thermodynamic constraints (Liang et al. 2004). Additionally, existing parameterizations do not represent the effects of mesoscale convective systems (MCSs), despite their large contributions to total rainfall in the tropics (Nesbitt et al. 2006). However, recent efforts have focused attention on characterizing aspects of mesoscale organization in convective parameterizations (Mapes and Neale 2011; Moncrieff et al. 2017), since computer resources will continue to limit our ability to explicitly resolve convection for global climate assessments for many years to come.

Factors controlling deep convection in the tropics include sensitivity to free-tropospheric moisture and entrainment profiles (Brown and Zhang 1997; Holloway and Neelin 2009; Schiro et al. 2016; Zhuang et al. 2018), the diurnal cycle (Betts and Jakob 2002; Chaboureau et al. 2004; Del Genio and Wu 2010; Zhang and Klein 2010), large-scale dynamics forcing vertical ascent (Kumar et al. 2013; Hohenegger and Stevens 2013), vertical wind shear (Rotunno et al. 1988), microphysical processes and aerosols (Andreae et al. 2004; Rosenfeld et al. 2008; Grabowski and Morrison 2017), and cold pools (Tompkins 2001; Khairoutdinov and Randall 2006; Böing et al. 2012; Schlemmer and Hohenegger 2014; Kurowski et al. 2018). Examining the transition to deep convection within a unified scheme (D'Andrea et al. 2014) and in varying spatiotemporal domains (Holloway and Neelin 2010; Adams et al. 2013) is also critical to our understanding. Ideally, a parameterization would yield realistic statistics for such processes across regions, seasons, times of day, and for varying levels of convective organization. Despite complexities, it is of interest to examine whether a bulk measure of buoyancy computed from a simple mixing parameterization can yield a consistent relation with observed deep convection over a range of conditions, including larger MCSs.

Several factors contribute to deep convective onset and associated uncertainty in GCMs, yet one of the most significant is thought to be the sensitivity to lower-free-tropospheric humidity and the entrainment profile (e.g., Hannah and Maloney 2011; Del Genio 2012; Oueslati and Bellon 2013; Kim et al. 2014). Sensitivity studies with climate models have demonstrated that the mixing processes in cumulus convection are among the most sensitive of parameters (Murphy et al. 2004; Klocke et al. 2011; Bernstein and Neelin 2016). Sahany et al. (2012) showed that differing the entrainment profiles in CAM3.5 had a substantial impact on the convective onset as defined by the entraining convective available potential energy (CAPE). Additionally, Kuo et al. (2017) found that without entrainment, the sharp increase in precipitation with column moisture observed over land (Schiro et al. 2016; Ahmed and Schumacher 2017) and ocean (Bretherton et al. 2004; Sobel et al. 2004; Peters and Neelin 2006; Holloway and Neelin 2009; Neelin et al. 2009; Del Genio et al. 2012; Ahmed and Schumacher 2015) and explored in theoretical and modeling studies (Raymond 2000; Sobel and Bellon 2009; Muller et al. 2009; Stechmann and Neelin 2011; Stechmann and Neelin 2014) disappears. Though the relation between convection and moisture is defined by a two-way interaction, Kuo et al. (2017) and others (e.g., Derbyshire et al. 2004; Hohenegger and Stevens 2013) have illustrated that moisture is an important precursor to convective onset via the effects of entrainment (Holloway and Neelin 2009; Schiro et al. 2016). However, detailed representation of cumulus mixing remains highly uncertain due partly to the lack of observational constraints, though mean-state biases in thermodynamic quantities critical to deep convective onset (e.g., Lintner et al. 2017; Gonzalez and Jiang 2017) may hinder success in representing deep convective processes even with improved physics.

By modifying the bulk entrainment profile, the relative roles of boundary layer humidity and free-tropospheric humidity can significantly change, which motivates our discussion here about the appropriate weighting of free-tropospheric and boundary layer air and the interaction between convection and the moisture field. Though there are many existing entrainment parameterizations with dependencies on cloud radius (Simpson and Wiggert 1969), height (Siebesma et al. 2003), boundary layer height (Soares et al. 2004; Siebesma et al. 2007), stochasticity (Raymond and Blyth 1986; Romps and Kuang 2010; Suselj et al. 2014), and vertical velocity (Neggers et al. 2002), here we investigate a "deep inflow" mixing assumption in which environmental air is incorporated in roughly equal proportions through a deep lower-tropospheric layer (Holloway and Neelin 2009).

Deep-inflow mixing is representative of a deep layer of environmental air mixing with a bulk deep convective updraft, likely via both small-scale turbulence and organized inflow [see Fig. 2 of Schiro et al. (2018) and discussion therein]. Holloway and Neelin (2009) and Schiro et al. (2016) explored the consistency of deep-inflow mixing assumptions to the observed onset of precipitation as a function of column water vapor (CWV) over a tropical ocean and tropical land site, respectively. Zhuang et al. (2018) extends this analysis to additional tropical and subtropical regions, concluding that the tropical ocean and Amazon sites are most sensitive to entrainment and the thermodynamics of the lower troposphere.

Missing from these studies, however, is a comprehensive assessment of the validity of deep-inflow mixing assumptions across a wide variety of environmental conditions and convection types.

Schiro et al. (2018) finds observational evidence of deep inflow into deep convective updrafts by relating empirical estimates of mass flux derived from radar wind profiler–derived vertical velocity to mixing assumptions. Such assumptions, when used to estimate buoyancy available to deep convection, yield a sharp increase in the probability of deep convection and precipitation rate as a function of buoyancy, deeming deep-inflow mixing an effective predictor of the onset of deep convection in the tropics. Ahmed and Neelin (2018) arrive at a similar answer using a different approach: to reverse engineer the influence of the environment, as contributed by various bulk layers (boundary layer, lower free troposphere, midtroposphere), analytically from the observed precipitation–water vapor relation shown in previous studies. Additionally, this strong buoyancy–precipitation relationship exists for both smaller-scale and larger, mesoscale convection (Schiro et al. 2018). Schiro et al. (2018) highlights how its formulation is independent of problematic (and highly tunable) mixing coefficients in current convective parameterizations. Both studies highlight the ability of a deep-inflow assumption to predict deep convective onset across both land and ocean regions in the tropics using TRMM 3B42 precipitation and ERA-Interim moisture and temperature.

Here, we extend the analysis of Schiro et al. (2016, 2018) to provide a detailed examination of variability in moisture vertical structure (regionally, diurnally, and seasonally; section 3), its relation to convective onset and convective organization (section 4), the effects of moisture on the conditional instability of the environment (section 5), and how an entrainment assumption that properly accounts for this moisture variability can be a successful predictor of deep convective onset (section 5). The convective environments in and around Manaus, Brazil, as intensively observed during the 2-yr Green Ocean Amazon 2014/15 (GoAmazon2014/5) campaign are the primary focus, since its moderate diurnal and seasonal moisture variability create a nice test case for evaluating the dependence of deep convection on boundary layer and lower-free-tropospheric moisture. We draw parallels where appropriate to the convective environment in the tropical western Pacific using data from the DOE Atmospheric Radiation Measurement (ARM) site at Nauru. The relationship between boundary layer and free-tropospheric moisture to convective onset is quantified, and plume buoyancies computed assuming deep-inflow mixing are compared to those computed with more traditional mixing assumptions and related to the observed onset of deep convection across regions, seasons, and times of day, and for varying degrees of convective organization.

2. Data

The data used in this study are taken from two DOE ARM sites in the tropics. The first is the DOE ARM Mobile Facility deployed as part of the GoAmazon2014/5 field campaign (January 2014–December 2015; Martin et al. 2016). All observations in this study were measured at the T3 site (3.21°S, 60.60°W, 50-m altitude) near Manacapuru, Brazil, except for data from an S-band radar at site T1 (3.15°S, 59.99°W) to the east of T3. The results from the GoAmazon2014/5 site are compared to 5 years of data (2001–06) from a retired DOE ARM site in the tropical western Pacific at Nauru (0.52°S, 166.9°E; 7-m altitude).

a. Moisture

Thermodynamic profiles and CWV data from the radiosondes were obtained from four- to five-times-daily launches (0130, 0730, 1030—wet season only—1330, and 1930 local time) at the GoAmazon2014/5 site (ARM Climate Research Facility 2013b) from Vaisala DigiCora III sounding systems at 2-s resolution (Holdridge et al. 2013). The raw sounding data were interpolated to 5-mb intervals (1 mb = 1 hPa) for mixing computations in section 5. The reported uncertainties are ~5% for relative humidity and ~0.5°C for temperature below 500 mb. At Nauru, launches occurred twice daily (0000 and 1200 LT). We remove any radiosondes from the analysis if rain occurred 4 h prior to launch to avoid, as best as possible, sampling within a cold pool and an environment modified by precipitation processes (though the results presented are robust to the inclusion of this threshold).

Microwave radiometer CWV from the GoAmazon2014/5 site using the microwave radiometer retrieval (MWRRET) value-added product (ARM Climate Research Facility 2013a) following procedures outlined in Turner et al. (2007) is employed in section 4. A linear interpolation procedure is performed to gap fill CWV values across time periods of 6 h or less. Interpolation is reasonable given that the data gaps are typically short and the temporal persistence of water vapor values for strong convective events is on the order of hours (Holloway and Neelin 2010), although quantitative differences can be noted between different methods of filtering and interpolation. Figure S1 in the online supplemental material quantifies these differences by comparing different interpolation methods and datasets, including those used in Schiro et al. (2016). The linear interpolation procedure likely underestimates peak CWV but is chosen as

a conservative method. The data used in this study are averaged at 12-min intervals to match the 12-min resolution of the Doppler radar.

b. Precipitation

In situ precipitation at the GoAmazon2014/5 site are from the Aerosol Observing System (AOS) and measured by the acoustic gauge of a Vaisala WXT520 meteorological station; these data are referred to as AOS surface meteorology (AOSMET) precipitation (ARM Climate Research Facility 2013c). When related to radiosonde CWV, AOSMET precipitation is averaged at 2-h intervals centered 1 h after radiosonde launch; this interval was found experimentally to be the most robust in capturing incidences of precipitation, given the limited spatial information. For analyses with radiometer CWV, AOSMET precipitation is averaged at 12-min intervals.

Radar-derived precipitation rates are also incorporated. These data were obtained from the Sistema de Proteção da Amazonia (SIPAM) ground-based S-band (10-cm wavelength), Doppler, single-polarized radar, with a horizontal beamwidth of 0.96° and a vertical beamwidth of 0.93° (Schumacher 2015). The radar scans up to 17 elevation angles from 0.9° to 19° every 12 min. The reflectivity data are interpolated to the constant altitude plan position indicator (CAPPI) data with a horizontal resolution of 2 km and a vertical resolution of 0.5 km (altitude ranges from 0.5 to 20 km). A single reflectivity–precipitation (Z–R) relation ($Z = 174.8R^{1.56}$), created using 2014 wet-season impact disdrometer data, was applied by ARM to the 2.5-km SIPAM Manaus S-band CAPPI data to generate rain rates for each radar volume (by C. Schumacher, Texas A&M). These data are then spatially averaged in 25- and 100-km grid boxes surrounding the GoAmazon2014/5 site (T3), to provide statistics comparable to that of typical GCM grid scales. Based on typical propagation speeds of convective cells in the Amazon (Vila et al. 2008), a 25-km gridbox average, for example, is representative of approximately 1-h temporal sampling. The 100-km grid box was shifted slightly right of center from the T3 site (i.e., closer to the location of the radar) as data are not recommended for use for rain rate retrievals beyond a 110-km radius of the radar.

c. Cloud-top height

Cloud-top height provides an additional measure of deep convection to the convective onset statistics presented in section 4. These data are obtained from a product provided through the DOE ARM program that uses the 95-GHz W-band ARM cloud radar (WACR), micropulse lidar, and ceilometer data to produce cloud boundaries using the WACR Active Remote Sensing of Clouds (WACR-ARSCL) value-added product (ARM Climate Research Facility 2014a,b). Cloud-top heights are averaged at 1-h intervals, and cloud tops with bases greater than 3 km are excluded from the analysis to isolate deep, convective clouds only.

d. Convection classification

Information about convection type is obtained from composite S-band radar reflectivity in a 100-km grid box surrounding the GoAmazon2014/5 site. Classifying deep convection and organized convection using radar data typically involves employing a maximum reflectivity threshold in base reflectivity (e.g., Churchill and Houze 1984; Steiner et al. 1995). If this threshold exceeds 40 dBZ, it is typically convective, as stratiform precipitation usually does not have such high base reflectivity. Here, we employ a threshold of 45 dBZ to distinguish convective from stratiform processes since we use composite reflectivity instead of base reflectivity. Events are grouped into four categories. Deep organized convection associated with MCSs is classified as having maximum reflectivity greater than or equal to 45 dBZ and a spatial extent greater than 50 km in one direction (see also Fig. 3 of Schiro et al. 2018). Spatial extent is defined by contiguous pixels with reflectivity greater than 30 dBZ. A 50-km threshold is employed here, rather than a more traditional 100-km threshold to identify mesoscale convective systems (Houze 2004), as a reasonable separation in order to include as many convective events as possible. We denote this as "mesoscale," noting the caveat that the spatial range 50–100 km is included. "Smaller scale" events are defined as the complementary set of convective events, with reflectivity greater than 45 dBZ but a spatial extent less than 50 km in one direction. These tend to be dominated by locally occurring isolated cells, but we use the term smaller-scale to emphasize that we have simply split the spectrum of deep-convective organization by spatial extent. Examples of mesoscale and smaller-scale events are shown in Fig. S2. Other precipitation (other) is defined by maximum reflectivity less than 45 dBZ for any spatial extent. Last, no precipitation (no precip) is defined by maximum reflectivity less than 20 dBZ throughout the 100-km domain.

3. Moisture vertical structure

A robust relationship exists between CWV and precipitation over tropical oceans (Bretherton et al. 2004; Peters and Neelin 2006; Neelin et al. 2009; Holloway and Neelin 2009; Ahmed and Schumacher 2015), which also holds over tropical land (Schiro et al. 2016; Ahmed and Schumacher 2017). This relationship depends on

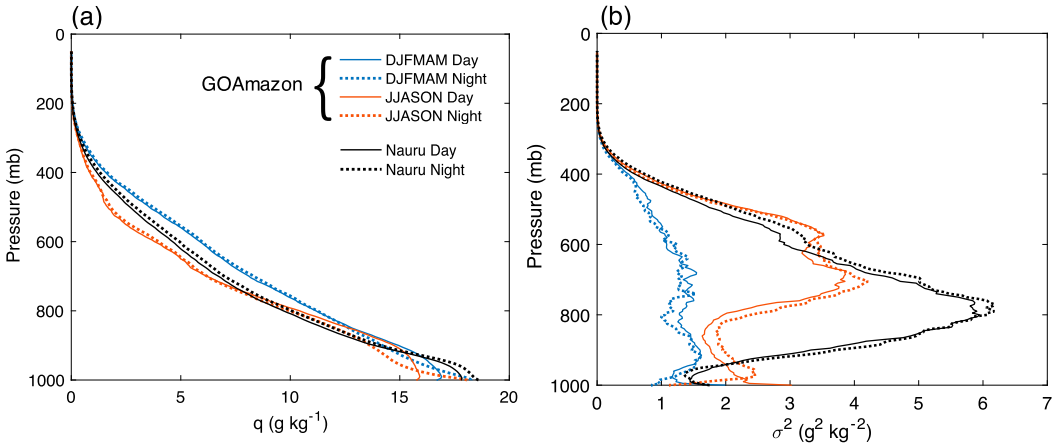

FIG. 1. (a) Mean specific humidity profiles averaged by time of day (nighttime: 0130, 0730, and 1930 local time; daytime: 1030 and 1330 local time) and season (DJFMAM in blue; JJASON in orange) at the GoAmazon2014/5 site. Profiles of specific humidity for Nauru are overlaid for comparison (black). (b) As in (a), but for specific humidity variance.

tropospheric temperature in ways that are more complex than saturation because of the key role of conditional instability associated with convection (Neelin et al. 2009; Sahany et al. 2012). In this study, we go beyond this relation by characterizing the effects of variability in moisture vertical structure regionally, seasonally, and diurnally on convective onset, in order to better understand the mechanisms through which the moisture field interacts with the convection through effects on conditional instability.

Figure 1 shows the mean moisture structure (Fig. 1a) and moisture variance profiles (Fig. 1b) throughout the troposphere for Nauru in the tropical western Pacific (black curve; see also Holloway and Neelin 2009) and the GoAmazon2014/5 site (color). The results shown at Nauru span the entire seasonal cycle, as there is little variability seasonally (see Fig. S3). There is also little variability in moisture diurnally, but we show this for reference. At the GoAmazon2014/5 site, we define seasons based on the two main patterns observed in moisture variance, seen in Fig. 1b. This definition varies from those traditionally used in the literature defining wet, dry, and transition seasons in the Amazon (e.g., Machado et al. 2004). Since we are specifically examining variability in moisture vertical structure and its effects on conditional instability of the environment and the onset of deep convection, the following definitions based on moisture variance prove useful. We use two seasons consisting of 6 months each—the wetter half of the year [December–May (DJFMAM)] and the drier half [June–November (JJASON)]—that will be compared throughout the study. Additionally, we group soundings into daytime (1030 and 1330 LT) and nighttime (0130, 0730, and 1930 LT) based on the similarities in their moisture variance profiles. This also aids in developing robust statistics, given the limited sampling of the radiosondes.

During the wetter months (DJFMAM), the atmosphere is moist throughout the entire troposphere and is less variable than the drier season (JJASON), wherein the humidity in the boundary layer and middle troposphere is more variable. Diurnal variability also exists in the vertical moisture structure, most notably in the near-surface layer but also in the lower free troposphere. Compared to Nauru, along the eastern margin of the warm pool in the tropical western Pacific, the boundary layer at the GoAmazon2014/5 site is less moist, but the lower free troposphere is moister. Moisture variance is notably greater at Nauru, particularly in the lower free troposphere, than it is at the GoAmazon2014/5 site.

Figure 2a shows the profiles of specific humidity conditionally averaged by CWV for Nauru (dashed), as shown in Fig. 3a of Holloway and Neelin (2009), over top of the results for GoAmazon2014/5 (solid). The results in Fig. 2a are averaged for all times of day and all seasons. For the same CWV values, the boundary layer humidity is higher at Nauru than at GoAmazon2014/5, and the lower free troposphere (~750–900 mb) is moister at GoAmazon2014/5 than at Nauru, especially at lower CWV. Above 700 mb, the GoAmazon2014/5 site still has higher humidity on average, but the profiles are more consistent across CWV. To summarize, the contribution to total CWV from the boundary layer at Nauru is larger, and thus the moisture content aloft is, on average, lesser at Nauru than it is at the GoAmazon2014/5 site for the same CWV. Thus, there are different moisture profiles with the same total column humidity over land and ocean, which likely contribute to differences observed

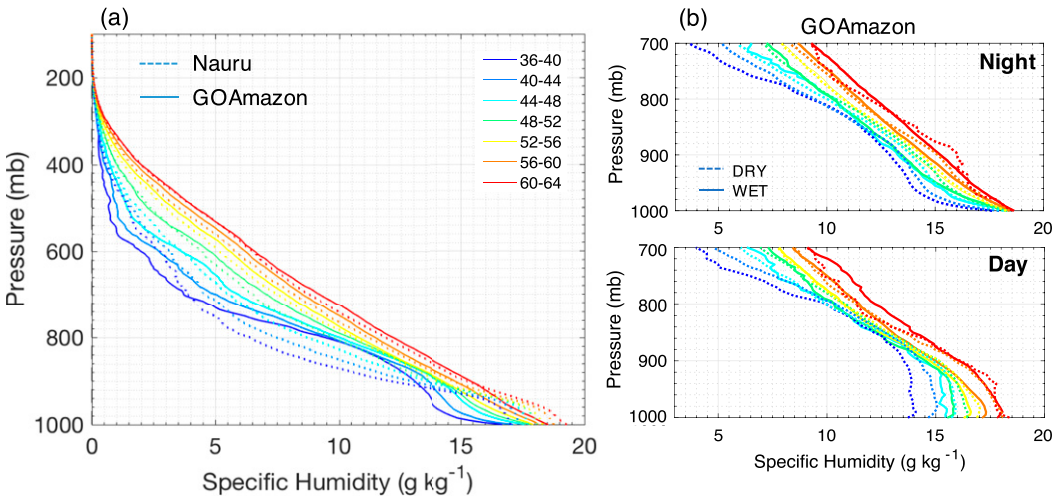

FIG. 2. (a) Specific humidity profiles averaged by CWV for Nauru (dashed) and GoAmazon2014/5 (solid). Averages are for profiles sampled four times daily at GoAmazon2014/5 and two times daily at Nauru across all seasons. (b) As in (a), but separated by season (wetter months: solid; drier months: dashed) and time of day [(top) night and (bottom) day] for GoAmazon2014/5 profiles only in the lower troposphere (700–1000 mb).

in the onset of deep convection as a function of CWV over land and ocean. For instance, the onset of deep convection occurs at lower CWV over land than ocean (Schiro et al. 2016; Ahmed and Schumacher 2017). This will be explored further in section 5 where we examine the effects of moisture on conditional instability with simple mixing parameterizations.

To examine the diurnal cycle and its relation to the moisture vertical structure in greater detail with respect to CWV at the GoAmazon2014/5 site, we conditionally average the specific humidity profiles on CWV of daytime and nighttime soundings for DJFMAM (solid) and JJASON (dashed) and zoom in on the structure in the lower troposphere (700–1000 mb) in Fig. 2b. Overall, the boundary layer in the daytime is deeper (on the order of 1 km), more variable, and spans a broader range of specific humidity values with CWV than in the nighttime boundary layer, which is much shallower (on the order of a few hundred meters), less variable, and spans a narrower range of humidity values with CWV. In the drier months, the boundary layer contributes more to the total column moisture than in the wetter months. In the drier months during the day, total column moisture is characterized by a narrower range of humidity values in the lower free troposphere than in the wetter months. Alternatively, above 700 mb, total column moisture is characterized by a broader range of humidity values in the drier months than the wetter months for both daytime and nighttime soundings (not shown). For reference, Fig. S4 in the supplement shows the correlation of CWV with specific humidity as a function of height separated by time of day and season. Mean temperature profiles were also examined at the GoAmazon2014/5 site (Fig. S5). Temperature variability is largely confined to the boundary layer, and temperature in the boundary layer is inversely related to the moisture content.

Associated implications of differences in moisture vertical structure (seasonally, diurnally, and across land and ocean sites) will be explored in greater detail in section 5 as we examine the relation between the moisture vertical structure and the conditional instability of the environment with entraining parcel models.

4. Convective onset statistics

a. Relationship to seasonal and diurnal cycles

The onset of deep convection, as shown by precipitation and cloud-top height as a function of CWV, is shown in Fig. 3 for DJFMAM day, DJFMAM night, JJASON day, and JJASON night. The statistics are shown for both in situ precipitation and precipitation from the S-band radar, as well as for CWV from both the microwave radiometer and radiosondes. Cloud-top heights are derived from the W-band cloud radar. All cloud tops with bases greater than 3 km are excluded from the statistics. It is evident that the conditional mean rain rate and cloud-top height, as well as the probability of precipitation exceeding 0.5 mm h^{-1} and cloud-top height exceeding 8 km, sharply increase with CWV across the diurnal and seasonal cycles.

During the daytime, precipitation is frequent, which is evident in the PDFs of precipitating points in comparison to the total points. On average, the onset is observed at slightly lower CWV in the daytime than at night

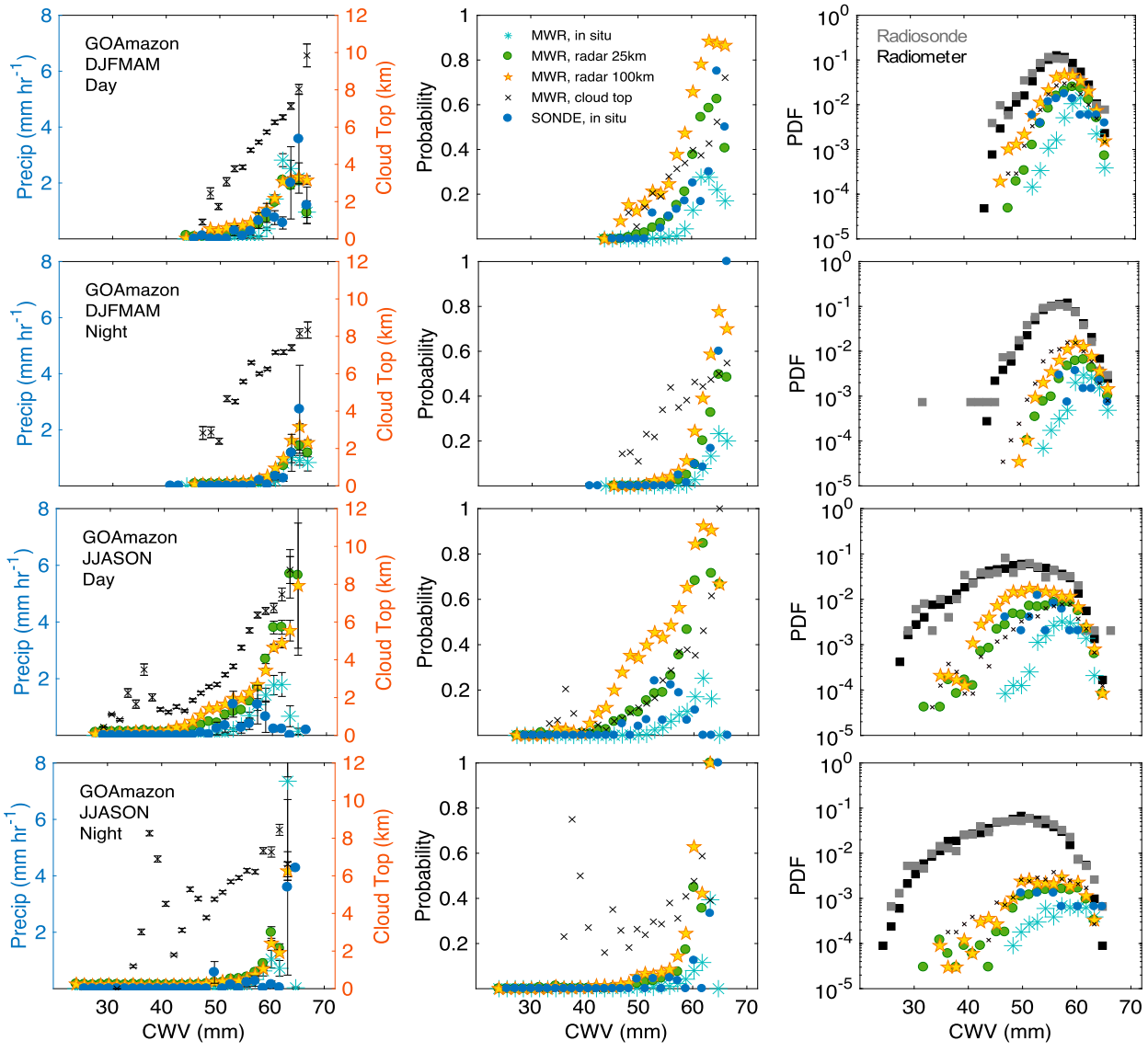

FIG. 3. Convective onset statistics at the GoAmazon2014/5 site for (first row) DJFMAM day, (second row) DJFMAM night, (third row) JJASON day, and (fourth row) JJASON night for 12-min-average microwave radiometer CWV and in situ precipitation (blue stars), radar precipitation within a 25-km grid box (green circles), radar precipitation within a 100-km grid box (yellow stars), and W-band cloud radar–derived cloud-top height (×), as well as radiosonde-derived CWV with 1-h average in situ precipitation (blue circles). (left) The precipitation conditionally averaged by CWV. (center) Probability of precipitation greater than 0.5 mm h^{-1} and cloud-top height greater than 8 km in each CWV bin. (right) The probability density of radiometer (black squares) and radiosonde (gray squares) CWV, and of precipitating points for each retrieval (colors).

(~55 mm in the daytime and ~60 mm at night for the wet season; onset defined loosely as the CWV value at the start of the sharp increase in conditional average in situ precipitation), and at higher CWV in the wetter months than in the drier months (~52 mm in the dry season vs ~59 mm in the wet season). Additionally, in the drier months, the range of CWV observed is wider than that observed during the wetter months. In the daytime, the lower-tropospheric moisture is higher than in the nighttime for the same CWV value and for the dry season in comparison to the wet season (Fig. 2). Knowing this, it is thus likely that differences in lower-tropospheric moisture content, rather than total column moisture, are most important to the onset of deep convection, thus contributing to the differences observed in the onset with respect to CWV regionally, seasonally, and diurnally. In section 4c, we go a step further and divide the lower troposphere into contributions from the boundary layer and free troposphere to examine their respective influences.

It is worth noting that these characteristics defining the onset are consistent across all observational platforms, yet the sampling limitation of the radiosonde and in situ–derived statistics in comparison to the radiometer- and radar-derived statistics is apparent. Throughout the remainder of the study, we use radiosonde-derived thermodynamic quantities in relation to in situ and radar precipitation, since we wish to examine the vertical moisture structure within the context of the conditional instability of the environment. Figure 3, however, provides some context for the robustness of the statistics when the sample size is increased.

b. *Convective organization*

To examine the onset as it relates to convective organization, radar data are employed to characterize the level of organization of the convection within a 100-km grid box surrounding the GoAmazon2014/5 site within an hour of radiosonde launches. As described in section 2d, convection is classified as deep if the composite radar reflectivity exceeds 45 dBZ. The convection is denoted as mesoscale when it exceeds 50 km in one linear dimension (contiguous reflectivity >30 dBZ), and smaller-scale for anything less than 50 km (see also Schiro et al. 2018). This information is displayed in a histogram in the left column of Fig. 4, with the probability of precipitation (precipitation rates greater than 0.75 mm h^{-1}) as a function of radiosonde-derived CWV overlain. Moving forward, all radiosondes launched after precipitation events up to 4 h prior are eliminated from this analysis to reduce the likelihood of sampling air directly modified by precipitation processes. Nevertheless, the results presented are robust to the inclusion of such a threshold. For the probability, only bins including five or more samples are plotted.

The information in Figs. 4a and 4b is complementary to that presented in Fig. 3: the probability of precipitation is the same except for being matched to radiosonde CWV and using 1-h averages of the radar data instead of 12-min averages, and the histogram presented is a more detailed look at the event type contributing to the distribution of precipitating points. The right column examines the fraction of the total observations that were classified as deep convection (all deep convection: gray stars; organized deep convection: red circles; cellular deep convection: blue squares). The gray stars share a symbol with the yellow stars in the left panel to signify their similarity, as the gray stars are derived from the classification at 100 km and the yellow stars are derived from reflectivity-derived precipitation in the 100-km domain.

The onset of deep convection occurs with increasing total moisture in the column (Figs. 4a,b). The average probability of precipitation is greater at 100 km than at 25 km and in situ because the likelihood of observing precipitation increases as the size of the grid cell increases [the quantitative increase depends on the spatial autocorrelation properties of the precipitation; values here are approximately consistent with satellite observations in Kuo et al. (2018)]. Isolated cells are the most common deep convection type, with mesoscale deep convection a larger fraction of the total at high CWV. A key finding is that the mesoscale deep convection and more local, smaller-scale convection are both sensitive to the humidity in the atmosphere, and the occurrence of both convective types sharply increases with increasing CWV. Smaller-scale convection is, however, observed at CWV in the 40–50-mm range, whereas the probability of organized convection picks up at higher CWV (~53–58 mm). This will be explored further in section 4c as a function of layer-mean moisture.

c. *Boundary layer versus free troposphere*

We now examine the respective relationships of boundary layer (chosen conservatively here to be between 950–1000 mb; ~450-m thickness) and free-tropospheric humidity (700–900 mb; ~2.1-km thickness) to deep convection and the spatial scales at which convection occurs. Much of the relation between deep convection and CWV can be explained by its relation to free-tropospheric moisture (Figs. 4c,d). Some of the relation can also be explained by boundary layer humidity (Figs. 4e,f), although this relationship is less pronounced on average. (For information about the sensitivity of these results to layer averaging, see Fig. S6 and corresponding discussion in the supplement.)

Figure 5 is the same as Fig. 4 for the free troposphere but separates out the analysis by time of day and season. The probabilities of precipitation for in situ, 25-km radar, and 100-km radar precipitation all increase sharply with increasing lower-free-tropospheric humidity for all seasons and times of day; the one exception is the dry-season nighttime (Fig. 5g), whose probabilities are lower (<25%). It appears for this case that high humidity in the lower free troposphere does not guarantee convection, but when convection is observed it occurs in humid environments only (roughly >21 mm). Additionally, the probability of both smaller-scale and mesoscale deep convection increases sharply with increasing humidity in the wet season (Figs. 5b,d). The same is true in the dry-season daytime, but there is a moderately high probability (>35%) of smaller-scale convection even for lower humidity (Fig. 5f). Isolated, cellular deep convection is ubiquitous throughout the domain during the daytime hours in all seasons and is the most frequent type of deep convection observed (Figs. 5a,e). At night, however, the probabilities of both convection types are equally likely (Figs. 5c,g) and increase sharply with increasing lower-free-tropospheric humidity (Figs. 5d,f).

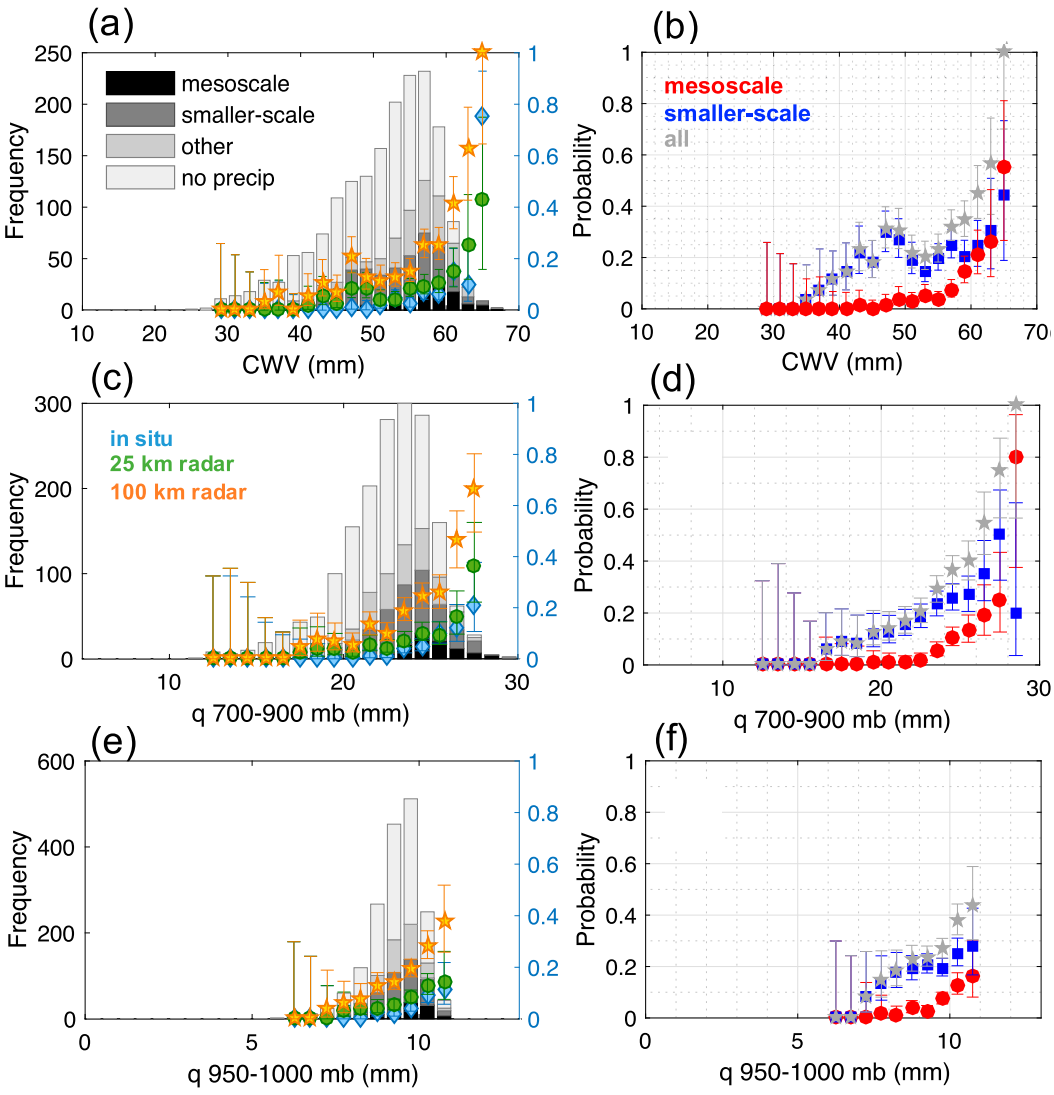

FIG. 4. (a),(c),(e) Histograms of convection type as classified using radar reflectivity and precipitation area within a 100-km grid box surrounding the GoAmazon2014/5 site (black: mesoscale deep convection ≥45 dBZ and at least 50 km wide in one direction; dark gray: smaller-scale deep convection ≥45 dBZ and <50 km wide in one direction; light gray: other precipitation with reflectivity <45 dBZ; white: no reflectivity signature ≥20 dBZ detected in the domain) and probability of precipitation greater than 0.75 mm h^{-1} from in situ rain gauge measurements (blue diamonds), radar precipitation within a 25-km grid box around the GoAmazon2014/5 site (green circles), and radar precipitation within a 100-km grid box around the GoAmazon2014/5 site (yellow stars) conditionally averaged by integrated humidity in (a),(b) the total column from 200 to 1000 mb, (c),(d) the lower free troposphere (700–900 mb), and (e),(f) the boundary layer (950–1000 mb). (b),(d),(f) The fraction of the total deep convective events (gray stars), smaller-scale deep convection only (blue squares), and mesoscale deep convection (red circles) with rain rates greater than 0.75 mm h^{-1}.

Overall, the occurrence of both smaller-scale and mesoscale convection is strongly tied to the lower-free-tropospheric humidity (Figs. 5b,d,f,h), with occurrence of smaller-scale convection at lower humidity in the daytime hours (particularly the dry season; Fig. 5f).

The role of the boundary layer is depicted in Fig. 6, where the probability of precipitation and frequency of deep convective events show a strong relation to the boundary layer humidity (1000–950 mb) during the daytime (Figs. 6a,b,e,f). At night (Figs. 6c,d,g,h), this relationship is less discernable. The nocturnal boundary layer, often shallower than 950 mb, is much less variable than the daytime boundary layer and maintains high humidity at nearly constant values. A layer of convective inhibition develops, and in some instances, is possibly a hindrance to the development of convection without the presence of mechanical lifting or erosion by solar heating in the morning hours. Smaller-scale convection

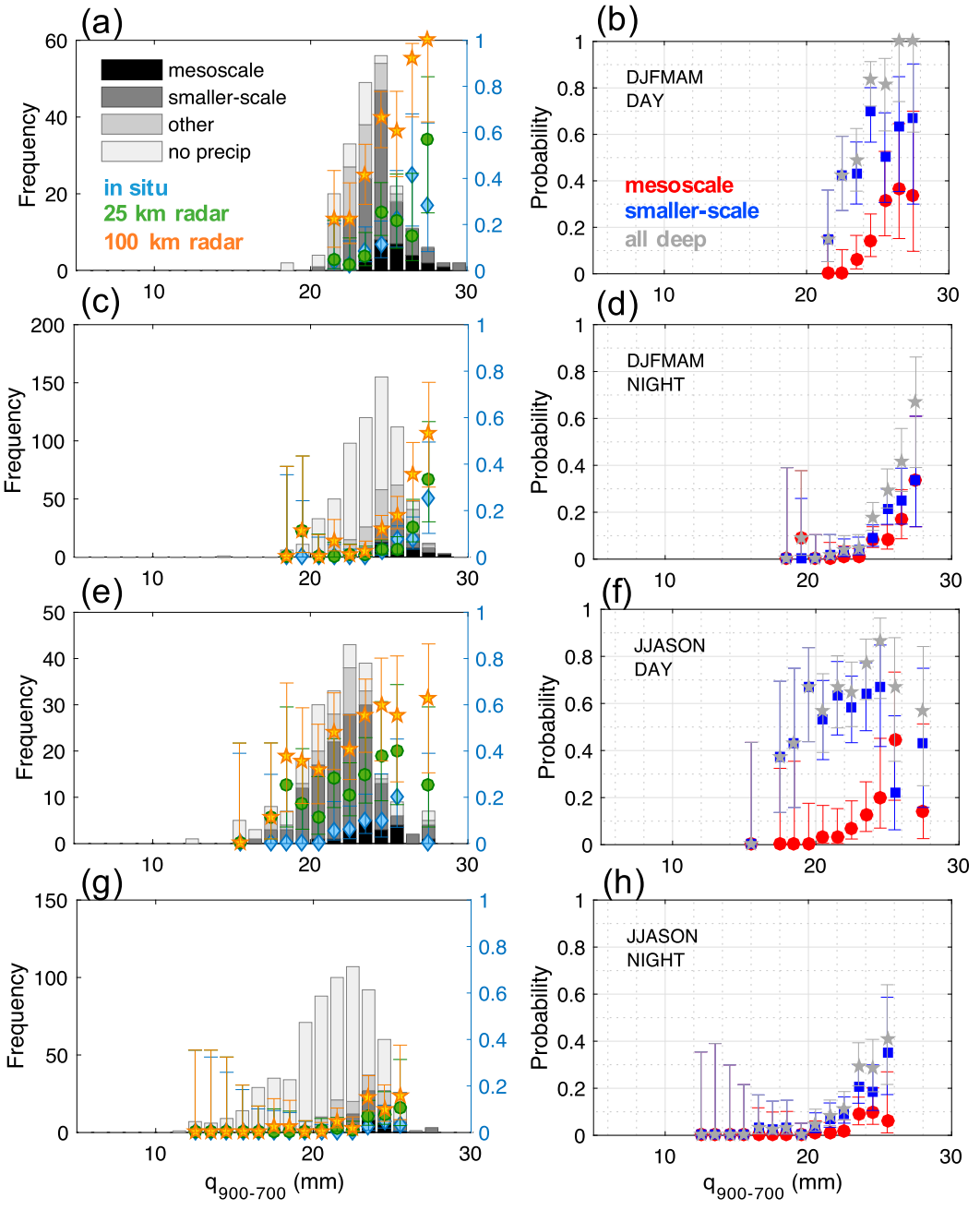

FIG. 5. As in Fig. 4, but for integrated humidity in the free troposphere (700–900 mb) only during (a),(b) DJFMAM day, (c),(d) DJFMAM night, (e),(f) JJASON day, and (g),(h) JJASON night.

increases sharply with increasing humidity during the daytime, while mesoscale convection does not appear to be as tied to the boundary layer humidity. Both the probabilities of precipitation (Figs. 6a,c,e,g) and the probability of deep convection (Figs. 6b,d,f,h) show that the relation to the boundary layer is much weaker during the nighttime than daytime.

Overall, deep convection of all types, in all seasons, and at all times of day occurs more frequently with increasing lower-free-tropospheric humidity. The occurrence of mesoscale deep convection appears most strongly tied to lower-free-tropospheric humidity. The boundary layer is also strongly related to convective onset, but this is mainly true for the daytime and smaller-scale convection only. This is consistent with what we know of diurnally forced convection over land (e.g., Nesbitt and Zipser 2003). For reference, variants of these statistics for the boundary layer and lower free troposphere are reproduced in the

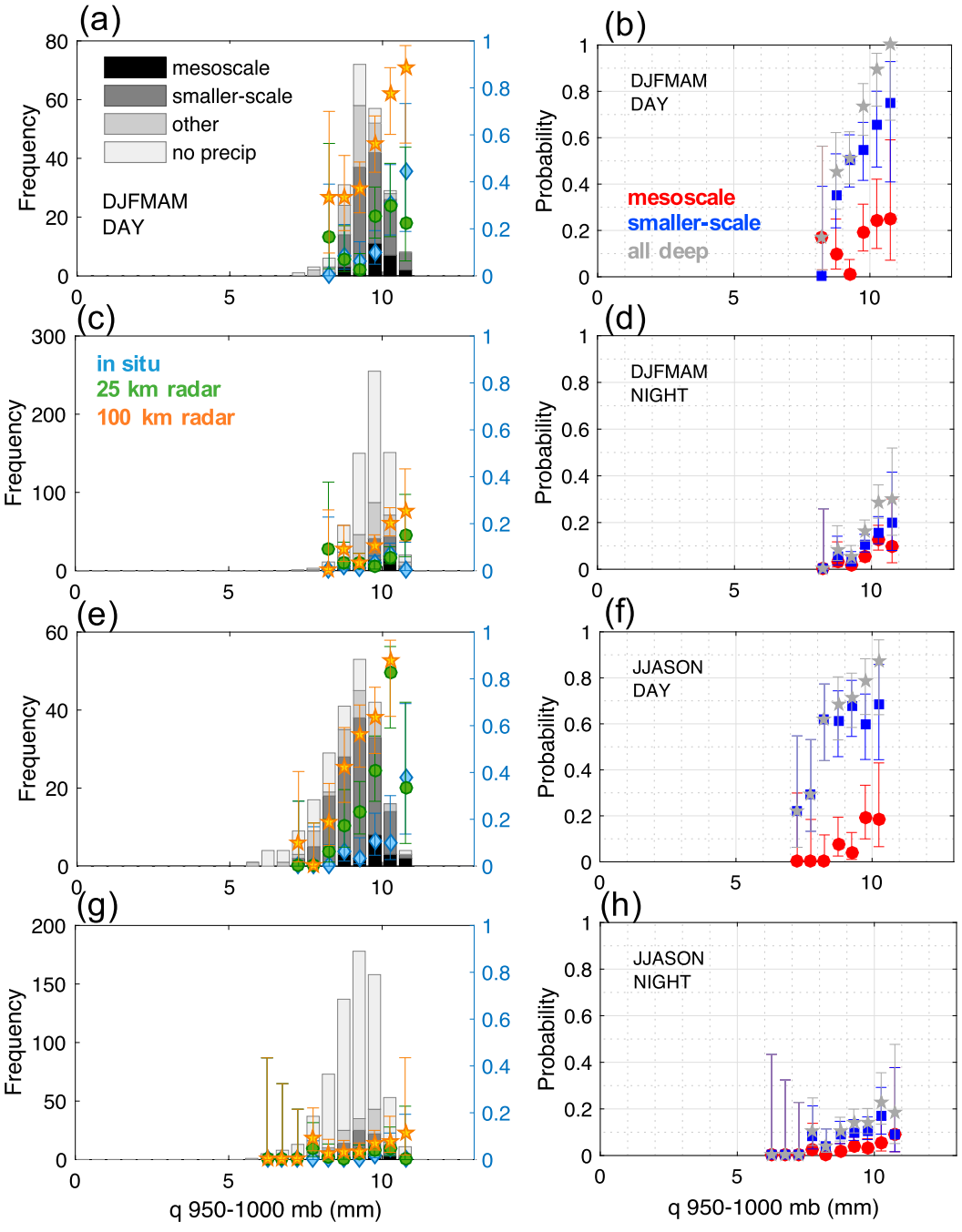

FIG. 6. As in Fig. 5, but for integrated humidity in the boundary layer (950–1000 mb).

supplemental material (Figs. S7 and S8) as a function of their respective layer saturation.

5. Relating observed deep convection to plume buoyancy under different mixing assumptions

In section 4, we examine the relation between deep convection and moisture and how variability in moisture vertical structure contributes to variability in deep convective onset as a function of total column moisture. It was also shown that both mesoscale and smaller-scale convection show a strong relation to lower-tropospheric moisture, particularly in the free troposphere. CWV has proven useful in previous studies since it is commonly available from GCM output and satellite retrievals (over ocean), and since it is a good proxy for conditional

instability over land and ocean (Holloway and Neelin 2009; Schiro et al. 2016). Here, since we have additional data available—vertical moisture structure and information about diurnal variability and convection type—we have the opportunity to test various assumptions of parcel buoyancy against observed deep convection across a range of conditions. Thus, in section 5, we refine our analysis by replacing CWV by measures explicitly based on the conditional instability of the environment, using different postulates for mixing as it affects plume buoyancy.

GCMs all make assumptions about buoyancy that, in combination with other parts of the deep convective closure scheme, yield precipitation. We thus ask how strong a relation to observed deep convection can be achieved with a single, physically consistent plume buoyancy formulation. We estimate plume buoyancy using the thermodynamic equation of a plume model [e.g., Masunaga and Luo 2016, their Eq. (10)], much like a GCM would in convective parameterization. The interpretation is necessarily done in the framework of convective plumes, but we note that we do not model plume vertical velocity dynamically (e.g., Masunaga and Luo 2016); rather, we constrain it with fixed assumptions of the total entrainment based on observational estimates (Schiro et al. 2018). Ideally, a bulk measure of buoyancy given a realistic, physically based assumption would show strong relation to observed precipitation and deep convection over a wide range of environmental conditions. Our exploration of thermodynamic controls in the previous section suggested that the consistent relation to lower-tropospheric moisture, particularly in the lower free troposphere, provides some indication that buoyancy is largely dependent on the moisture available in this layer, and that a model of plume buoyancy that adequately accounts for variability in this quantity could yield consistent results under a range of environmental conditions (e.g., across seasons, diurnal cycle, regions, and even for different convection types).

Deep-inflow mixing (Holloway and Neelin 2009; Sahany et al. 2012; Schiro et al. 2016, 2018) is a term we adopt to describe mixing formulations that assume updraft mass flux in deep convection increases nearly linearly through a deep lower-tropospheric layer. A combination of observational and numerical results in the literature suggests that this layer can commonly be 3–4 km thick (Lucas et al. 1994; Robe and Emanuel 1996; Kingsmill and Houze 1999; Mechem et al. 2002; Wang and Liu 2009; Mrowiec et al. 2012; Yeo and Romps 2013; Kumar et al. 2015, 2016; Giangrande et al. 2016; Schiro et al. 2018), though the depth can be smaller, possibly dependent on storm dynamics and the thermodynamic environment (e.g., Mechem et al. 2002), and there exist examples of exceptions to this behavior (Anderson et al. 2005; Mishra and Srinivasan 2010; Zhu 2015; Yang et al. 2016). Schiro et al. (2018) find details of the vertical shape of the mass flux and depth of the layer are less important, so long as the inflow produces an updraft with bulk properties of a lower-tropospheric layer rather than a surface parcel. Evidence of ''layer lifting'' in modeled (Mechem et al. 2002) and observed (Kingsmill and Houze 1999) mesoscale convective systems is suggestive of the role of coherent structures in deep-inflow mixing. Deep-inflow mixing can also be inferred from mass flux profiles (LeMone and Zipser 1980; Robe and Emanuel 1996; Yeo and Romps 2013; McGee and van den Heever 2014; Kumar et al. 2015, 2016; Giangrande et al. 2016; Schiro et al. 2018), although this does not distinguish between the roles of coherent structures versus turbulence. We note that the deep-inflow framework is agnostic to the mechanism through which the air becomes incorporated into the plume (e.g., it could occur partly through organized inflow at the plume scale or mesoscale in addition to small-scale turbulence).

It is reasonable to conjecture that this scheme might apply to the mesoscale-organized convection identified in the analysis above, in addition to smaller-scale deep convection. Schiro et al. (2018) highlight the physical interpretation of such an assumption, its estimation from radar-derived mass flux, ways in which this helps to reframe a problematic dependence on tunable coefficients in convective parameterizations, and its validity for both mesoscale and smaller-scale deep convective structures. Here, we are able to examine its validity over the seasonal and diurnal cycle and for mesoscale and smaller-scale convection in the Amazon given the extensive suite of instrumentation deployed as part of the GoAmazon2014/5 campaign, an otherwise difficult task using large, gridded datasets.

a. Formulation

If detrainment is neglected, an entrainment profile can be calculated for any corresponding mass flux profile from mass continuity. We can derive mixing coefficients $\chi_k = -m^{-1}(\partial m/\partial p)\Delta p$, where m is the mass flux, p is pressure, and k is the pressure level, with Δp defined to be positive. Though we demonstrate that local mixing coefficients can be calculated from a mass flux profile here, it is not necessary to perform the calculation and estimate buoyancy in this way (see also Schiro et al. 2018). If mass flux increases with height throughout the lower troposphere, this would suggest large lower-tropospheric entrainment rates. The weighting of the conserved environmental variable $\tilde{r}$, or the influence function $I(z_B, z)$ of the environment on the properties of

the updraft r at height z_B, is given by the vertical rate of increase of mass:

$$r(z_B) = \int_{z_0}^{z_B} I(z_B, z)\tilde{r}(z)\,dz \approx \frac{1}{m(z_B)}\int_{z_0}^{z_B} \tilde{r}\frac{\partial m}{dz}dz. \quad (1)$$

Schiro et al. (2018) note the derivation of this for layer integrals that may be robust to nonlocal mixing, but it is consistent with the common local mixing formulation $\partial r/\partial z = \epsilon(\tilde{r} - r)$ (the change in a conserved quantity with height) and mass continuity combined in pressure coordinates and integrated over pressure. If the plume's mass is increasing linearly with height, this reduces to a vertical average of all levels $r(z_B) = (z_B - z_0)^{-1}\int_{z_0}^{z_B}\tilde{r}\,dz$, with $I(z_B, z)$ constant in height. This corresponds to a local mixing of $\epsilon = z^{-1}$. The influence function helps to clarify that a weighted vertical average of lower-tropospheric thermodynamic properties affecting buoyancy arises naturally from entraining plumes that grow with height through a lower-tropospheric layer in a way that is more difficult to see from a traditional parcel model, even though the deep inflow can be mathematically mapped onto a parcel-like computation for numerical and comparison purposes. It is worth underlining that a constant or slowly varying influence function removes the need for a disproportionately influential initial parcel.

Though we implement two specific assumptions of deep-inflow mixing here ("deep-inflow-A" and "deep-inflow-B"), we do not limit our definition of deep-inflow mixing to these specific schemes. Deep-inflow-A (Holloway and Neelin 2009; Sahany et al. 2012; Schiro et al. 2016) is given from an LES-based estimate of the vertical dependence of the mixing coefficient reported in Siebesma et al. (2007), where the mixing coefficient has an inverse dependence on height following $\chi_k\Delta p = c_\epsilon z_k^{-1}\Delta z_k$, where $c_\epsilon = 0.4$, z is the height, and Δz_k is the depth of the layer. Deep-inflow-B uses an idealized updraft vertical velocity that increases nearly linearly with height with $0\,\mathrm{m\,s^{-1}}$ at 1000 hPa and its maximum at 7 km (430 hPa). This shape profile was chosen based on observed profiles from aircraft campaign data (e.g., LeMone and Zipser 1980) and radar wind profiler observations of vertical velocity (e.g., Giangrande et al. 2016; Schiro et al. 2018). In Schiro et al. (2018), observations of vertical velocity are composited for both smaller-scale and mesoscale systems, showing that for both types of systems, the mass flux increases nearly linearly through a deep lower-tropospheric layer, motivating the assumptions for the mass flux profile in deep-inflow-B here. The mixing coefficients are computed from the vertical gradient of the specified updraft vertical velocity profile, with the mixing coefficient set to zero above 7 km (under the postulate that there is negligible mixing above the level where mass flux no longer increases). Entrainment in both deep-inflow-A and deep-inflow-B scale as z^{-1}, yet there is some evidence in the literature pointing to the importance of other scaling (e.g., Romps 2010; Hernandez-Deckers and Sherwood 2018).

Here, we analyze four different mixing scenarios for a rising plume: (i) no mixing, (ii) constant mixing at a rate of $0.001\,\mathrm{hPa^{-1}}$ (Brown and Zhang 1997; Holloway and Neelin 2009; Sahany et al. 2012), (iii) deep-inflow-A mixing, and (iv) deep-inflow-B mixing. Though our conceptual framework for mixing is applicable to rising plumes, the computations can be mapped onto those of a parcel model. Thus, we will describe the physics within a rising plume framework throughout, though the mixing is computed as follows:

$$r_k = (1 - \chi_{k-1}\Delta p)r_{k-1} + \chi_{k-1}\Delta p\tilde{r}_{k-1}, \quad (2)$$

where r is the conserved variable (ice–liquid water potential temperature), $\tilde{r}$ is the corresponding environmental variable, k is the pressure level, Δp is the pressure interval, and χ is the mixing coefficient. For all mixing assumptions that include freezing, liquid water is converted to ice conserving the ice–liquid water potential temperature when the plume reaches 0°C and latent heat is released into the plume. All parcels originate at 1000 mb, and buoyancy is computed between 1000 and 200 mb in this analysis (unless otherwise noted). All computations are performed in pressure coordinates. For reference, a case with no mixing is also shown.

Though highly simplified, the rising parcel proves useful for testing consistencies between buoyancies estimated from a variety of mixing assumptions and the occurrence of deep convection using field campaign observations. However, as previously mentioned, we do not necessarily advocate for the use of parcel-based methods in GCM parameterization. Though we choose to implement deep-inflow mixing into our current analysis using traditional methods, the deep-inflow framework is one in which bulk lower-tropospheric thermodynamics represent the influence of the environment on plume buoyancy, regardless of the exact mathematical implementation in parameterization (Schiro et al. 2018).

b. Profiles

Figure 7 compares the calculated buoyancy profiles between the GoAmazon2014/5 site and Nauru for the range of mixing assumptions described above and examines their consistency to the onset of deep convection observed with increasing humidity. All profiles are virtual temperature profiles derived from the radiosondes. Environmental profiles are subtracted from the plume

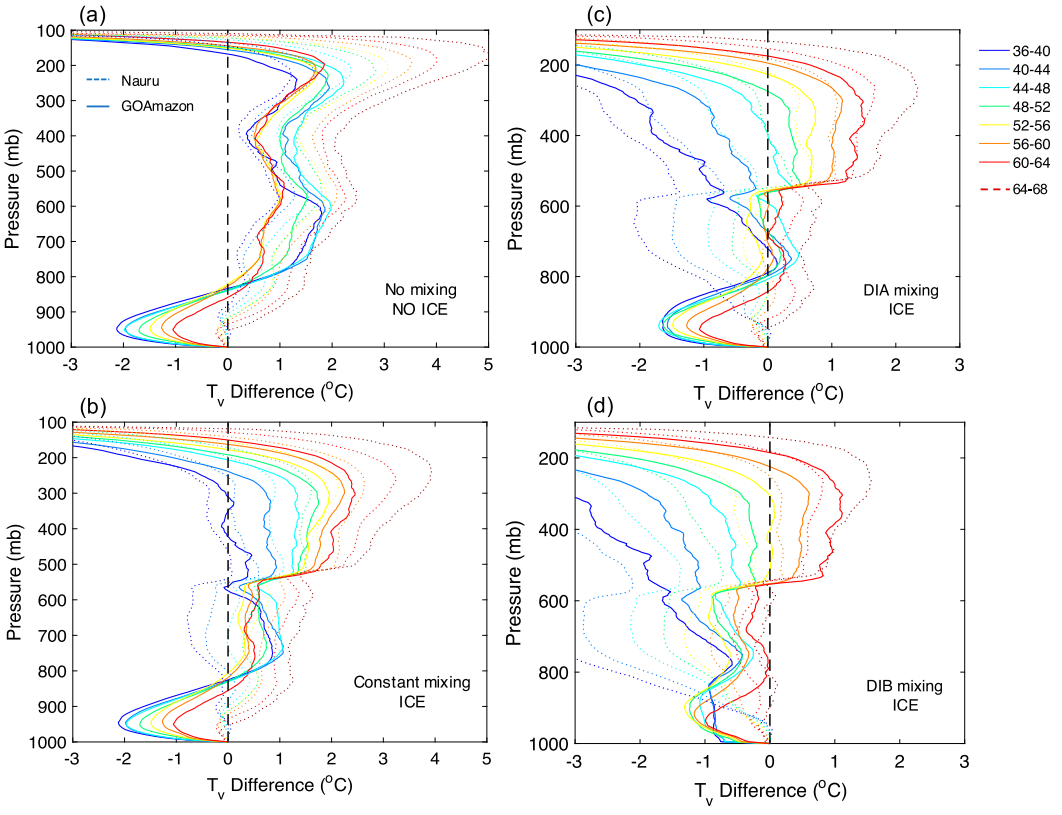

FIG. 7. Mean virtual temperature differences between plumes originating at 1000 mb and their surrounding environments conditionally averaged by CWV for (a) no mixing, (b) constant mixing (0.001 hPa^{-1}), (c) deep-inflow-A mixing, and (d) deep-inflow-B mixing for Nauru (dashed) and GoAmazon2014/5 (solid).

computations, which originate at 1000 mb (near surface). Profiles in Fig. 7 are averaged for all times of day and all seasons. These profiles can be directly compared to Figs. 1 and 2 in Schiro et al. (2016), which are figures illustrating the onset of precipitation as a function of CWV; for example, if buoyancies are generally positive in our experiment here, that should correspond to observed precipitation rates greater than 0 within that CWV bin. It is worth noting again that, unless separated by time of day, the analysis at the GoAmazon2014/5 site will be more representative of the nighttime soundings than the daytime soundings because of a higher frequency of nighttime soundings.

Figure 7a is the simplest case, which assumes no mixing with the surrounding environment, and thus the buoyancies are largely dependent on the characteristics of the plume at its level of origin. This yields results inconsistent with the onset of precipitation at a critical value of CWV (e.g., Fig. 4 herein; see also Fig. 3a in Holloway and Neelin 2009; Fig. 2a in Schiro et al. 2016) over both land and ocean, since buoyancies are positive through the free troposphere for all CWV at Nauru and GoAmazon2014/5 (above a layer of convective inhibition in the nighttime hours at GoAmazon2014/5). This would imply conditional instability available to deep convection, even under CWV conditions for which little occurs. Additionally, at the GoAmazon2014/5 site, the lower-CWV cases are more buoyant than the higher-CWV cases. This is largely because, on average, 1000-mb moisture is similar across CWV values at GoAmazon2014/5, yet the free troposphere is cooler on average for lower CWV (not shown). This means that the parcel originating at 1000 mb starts off just as buoyant as the high-CWV parcels, but then travels through cooler, denser air aloft, enhancing parcel buoyancy. The excessive buoyancy for this case occurs even without the inclusion of freezing, which tends to enhance buoyancy in the upper troposphere.

In comparison to the no-mixing case, the constant-mixing case shows some improvement in matching buoyancy with the onset of precipitation in that the buoyancy is small or negative for the lowest CWV values at both Nauru and GoAmazon2014/5 (Fig. 7b). For the GoAmazon2014/5 site, the inverse relationship between buoyancy and CWV seen in the 600–800-mb layer is still apparent, yet there exists a consistent relation to CWV in the layers above. In these figures, the rapid-freezing

assumption allows the contribution of the latent heating of freezing to buoyancy at upper levels to be easily seen; more gradual freezing would spread this increase across the layers above. If freezing is not included, this scheme would appear more consistent with the pickup in precipitation at Nauru (Holloway and Neelin 2009). With freezing, it suggests conditional instability through a deep layer even for fairly low values of CWV.

Figures 7c and 7d show that including inflow from a substantial lower-tropospheric layer using deep-inflow mixing yields a more robust relationship between plume buoyancies calculated and the sharp increase in precipitation observed with increasing CWV (Holloway and Neelin 2009; Schiro et al. 2016) than the other relations in Figs. 7a and 7b for both land and ocean cases. In other words, plume buoyancies are generally negative throughout the column for CWV values at which precipitation is not observed and positive for values of CWV at which precipitating events are observed (see Schiro et al. 2016, Figs. 1 and 2 therein). It should be noted that these calculations can be sensitive to microphysical assumptions (not shown), such as the removal of condensate within the calculation, which can increase (decrease) buoyancies in the lower to middle (upper) troposphere (Zhuang et al. 2018). Overall, for a plume originating from the boundary layer, mean plume buoyancies with respect to CWV are most consistent with the sharp increase in precipitation observed throughout the depth of the troposphere for assumptions that include substantial mixing through a deep lower-tropospheric layer over both land and ocean.

In a complementary study, Ahmed and Neelin (2018) reverse engineer an idealized mass flux profile from the observed water vapor–precipitation relation using reanalysis and satellite data, which increases nearly linearly in height throughout the lower troposphere. They find that precipitation increases sharply with increasing buoyancy (computed using the deep-inflow assumption derived) over both land and ocean regions in the tropics. Though different approaches, the results presented in Fig. 7 and those of Ahmed and Neelin (2018) suggest that the CWV–precipitation relation is primarily a function of variability in moisture in the lower troposphere over land and ocean, and that entraining plume buoyancies are most realistic when such variability is appropriately considered in entrainment assumptions.

Figure 8 examines the GoAmazon2014/5 case in greater detail. Since there is more variability in the moisture vertical structure as a function of time of day and season at this site, we can gain insight from how moisture variability affects buoyancy and thus the onset of deep convection. We examine this in Fig. 8 by checking for consistency between the observed moisture–precipitation relations (Fig. 4) and the onset as given by the buoyancy profiles. Results are shown for buoyancies computed using constant mixing with freezing ($0.001\,\mathrm{hPa}^{-1}$; dashed lines) and deep-inflow-B with freezing (solid lines) for plumes originating at 1000 mb. The onset occurs at lower total CWV in the dry season than the wet season, and in the daytime compared to nighttime, as is shown in Fig. 3. This is most likely a result of the greater moisture in the boundary layer and lower free troposphere for the same CWV values (see Fig. 2), yielding more buoyancy.

For the case of constant mixing, the boundary layer and lower free troposphere are treated unequally, placing greater weight on the boundary layer. The constant-mixing case appears to be too buoyant (in the sense that it predicts deep conditional instability at CWV values for which little precipitation is observed) at all times. Increasing the entrainment coefficient helps to a certain extent (see Fig. S9), but since it decreases buoyancy relatively uniformly throughout the whole column, rather than enhancing mixing in the lower troposphere only, there is an upper limit to the coefficient before significantly reducing buoyancy above the freezing level to values no longer consistent with deep convection. Raising the parcel from above the boundary layer also reduces the spurious prediction of deep conditional instability at intermediate CWV values to some degree (see Fig. S10), although it is unphysical to assume a parcel originates from 925 mb all the time. Overall, the constant-mixing case is limited in its representation of diurnal and seasonal variability in convective onset as a function of CWV. This suggests that its weighting of lower-tropospheric air, placing greater emphasis on boundary layer air, is not optimal.

For the deep-inflow-B mixing case, which accounts for nearly equal weighting of boundary layer and lower-free-tropospheric humidity, the range of CWV values at which the plumes become positively buoyant ($\Delta T_v > 0$) is generally consistent with the approximate CWV values at which the onset can be observed in Fig. 3 for all times of day and seasons. While we are careful not to suggest this as the optimal weighting, we note that mixing of such proportions can capture diurnal and seasonal variability in buoyancy consistent to the observed onset. However, Schiro et al. (2018) found that varying the details of the weighting of the lower free troposphere and boundary layer air are insignificant to the relation to the onset of deep convection, so long as the contribution from the lower free troposphere is substantial. The ratio of free-tropospheric moisture to boundary layer moisture varies seasonally and diurnally (Fig. 2), but the consistency between the observed onset and deep-inflow mixing suggests that this variability appears less important than the total moisture content.

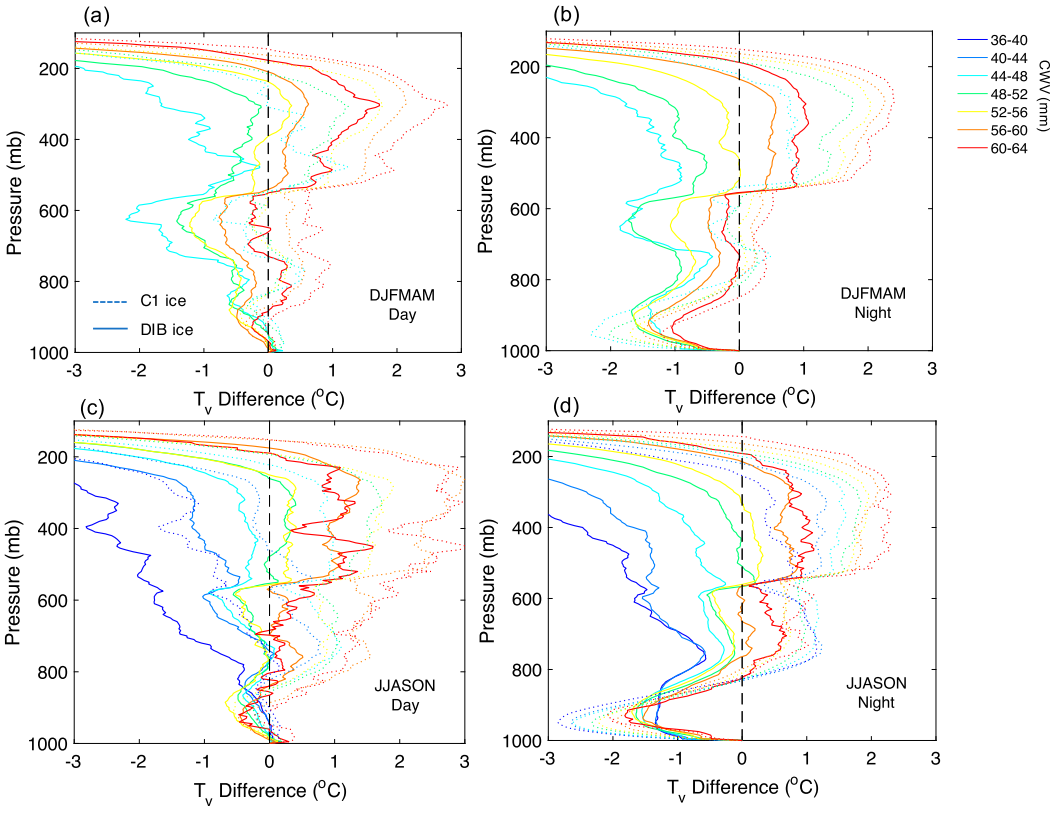

FIG. 8. Mean virtual temperature differences between plumes originating at 1000 mb and their surrounding environments conditionally averaged by CWV for deep-inflow-B (solid) and constant 0.001-hPa^{-1} (dashed) mixing with ice at the GoAmazon2014/5 site for (a) DJFMAM day, (b) DJFMAM night, (c) JJASON day, and (d) JJASON night.

In other words, the deep-inflow scheme appears to be giving sufficient weight to lower-free-tropospheric moisture, consistent with its importance as a key thermodynamic variable controlling convective onset. It should also be noted that though temperature variability can contribute significantly to plume buoyancy, it tends to be inversely related to specific humidity in the lower troposphere in the Amazon (Fig. S5), and is not a primary control on deep convection, as indicated by buoyancy calculations in which temperature and moisture are held fixed in turn (Fig. S11; see also Zhuang et al. 2018).

Surely for some optimal constant value, at some optimal level in the atmosphere at which buoyancy is evaluated (e.g., cloud-top height, without freezing; Brown and Zhang 1997)—depending also on the microphysical assumptions—one could argue that a constant-mixing assumption could work well. The problem, however, is that this constant is nearly impossible to observe and is difficult to deduce from modeling experiments. The deep-inflow assumption, on the other hand, is consistent with the presented (and preexisting) evidence surrounding the influence of lower-free-tropospheric humidity on convection, relatively insensitive to its exact formulation, and simplifies an otherwise complex dependence on tunable coefficients (Schiro et al. 2018). For reference, local entrainment coefficients used here are shown for the lower free troposphere in Fig. S12 of the supplemental information, along with influence functions for deep-inflow cases.

c. *Onset of deep convection as a function of buoyancy*

We now examine how strong a relation to observed deep convection an integral measure of buoyancy can yield. For simplicity, we use the mean parcel buoyancy $[B = g(T_{v,p} - T_{v,e})/T_{v,e}]$ from 200 to 1000 mb as the integral measure, since we want to consider a quantity that transitions smoothly from negative to positive and includes both the lower and upper troposphere. Schiro et al. (2018) found that the relation between the integrated buoyancy and the onset of deep convection is largely insensitive to the choice of layer through which the buoyancy is integrated. Figure 9 shows the histograms of convection type, probability of precipitation, and probability of observing mesoscale and smaller-scale

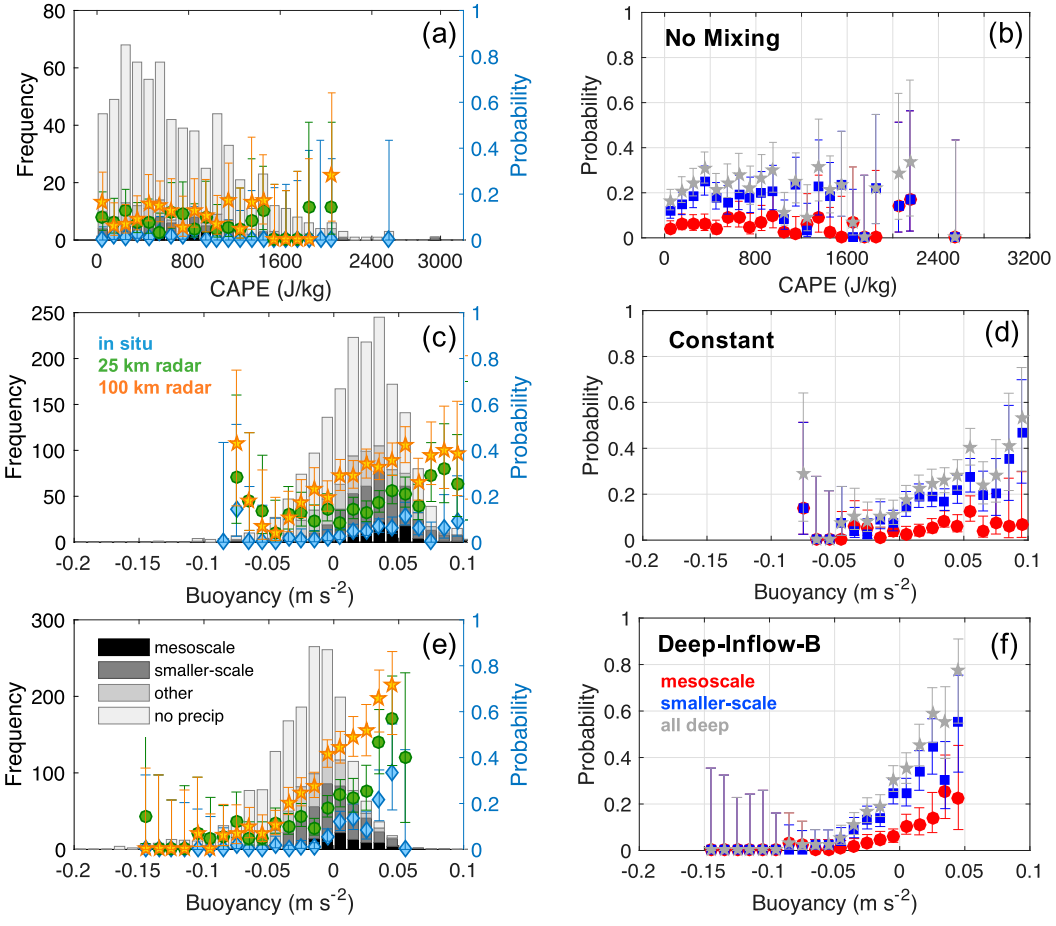

FIG. 9. As in Fig. 4, but binned by buoyancy computed with the following assumptions: (a),(b) CAPE computed irreversibly, (c),(d) constant mixing at 0.001 hPa^{-1} with freezing, and (e),(f) deep-inflow-B mixing with freezing.

convection as a function of buoyancy computed with three different assumptions of mixing: (i) no mixing, using the traditional convective available potential energy [CAPE $= \int_{\mathrm{LFC}}^{\mathrm{LNB}} g(T_{v,p} - T_{v,e})/T_{v,e}\, dz$, where LNB is the level of neutral buoyancy, LFC is the level of free convection, $T_{v,p}$ is the parcel virtual temperature, $T_{v,e}$ is the environmental virtual temperature, and g is the acceleration due to gravity] computed irreversibly without mixing; (ii) constant mixing (0.001 hPa^{-1}) with freezing (Fig. 9b); and (iii) deep-inflow-B mixing with freezing (Fig. 9c). Given that layer-integrated water vapor quantities exhibit strong relations to a pickup in precipitation probability, we seek a buoyancy-based calculation showing at least as strong a relationship.

Precipitation probability conditioned on buoyancy computed using a deep-inflow mixing assumption indeed yields a strong pickup above a threshold value. In this sense, deep-inflow-B buoyancy can be termed a good predictor for precipitation probability. Both the strong increase in probability of precipitation at high buoyancy values, as well as the high probability of no precipitation that can be inferred at low buoyancy values, could be equally helpful for model diagnosis. Precipitation probability conditioned on buoyancy computed using no mixing (see also Fig. S13) or constant mixing yield less strong relationships. As mentioned previously, increasing the entrainment coefficient in the constant-entrainment case helps somewhat, but increasing it too much tends to shift the entire plot toward negative buoyancy (not shown). Buoyancies start becoming strongly negative before a relation that closely resembles that between precipitation and buoyancy from deep-inflow mixing emerges.

We then explore the potential utility of deep-inflow mixing as a predictor of precipitation probability across seasons and times of day in Fig. 10. We conjecture that since there is a strong relationship to 700–900-mb humidity across the diurnal and seasonal cycles (Fig. 5), an assumption that more heavily weights the contribution of the lower free troposphere to buoyancy will show a more consistent relation to the probability of precipitation. Figure 10 also examines the utility of a deep-inflow

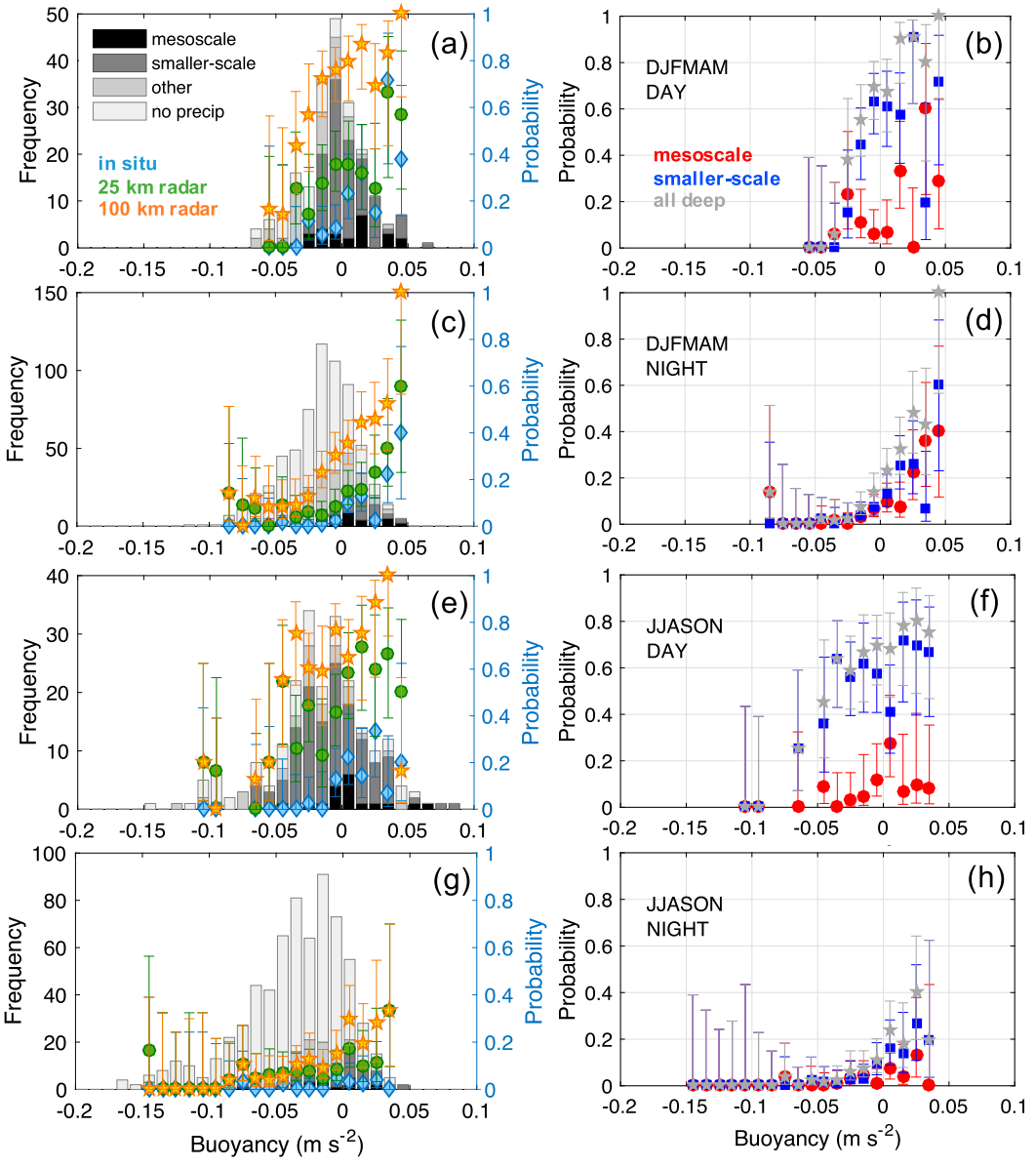

FIG. 10. (left) Probability and frequency of precipitation and deep convection conditionally averaged by buoyancy for (a) DJFMAM day, (c) DJFMAM night, (e) JJASON day, and (g) JJASON night. (right) Probability of all deep convective events (gray stars) as determined by the fraction that are mesoscale (red circles) vs smaller-scale (blue squares) for (b) DJFMAM day, (d) DJFMAM night, (f) JJASON day, and (h) JJASON night. Buoyancies are computed with deep-inflow-B mixing, and all condensate is frozen at 0°C.

assumption as a predictor of deep convection occurring in mesoscale systems versus smaller-scale convection. One can ask whether buoyancy based on a single mixing parameterization can yield strong relationships to the probability of precipitation for both larger mesoscale and local smaller-scale convection across the seasonal and diurnal cycles, a difficult task.

For all deep convection (gray bars) in Fig. 10, this holds reasonably well: there is always a transition from low probability of precipitation at negative values of the estimated buoyancy to higher probability in the vicinity of zero or above. We note the caveat that the jump to higher probability in the dry-season daytime occurs at negative values of the buoyancy estimate and has substantial error bars. With the caveat that the number of samples is modest in some panels of Fig. 10 and the pickup for mesoscale systems is clearest at night, the relation between plume buoyancy computed with deep-inflow mixing and both mesoscale and smaller-scale convection tends to hold across the seasonal and

diurnal cycles in the Amazon. This is suggestive of a single scheme's applicability, at least as a first approximation, to both convective types for convective closure and the potential to alleviate biases in the diurnal cycle of convection and precipitation over land. Moreover, using a mixing assumption that includes sufficient mixing from the lower free troposphere and has no explicit dependence on a tunable mixing coefficient (Schiro et al. 2018), a similarly strong relation to that of deep convection and humidity is captured by an integral buoyancy measure.

6. Conclusions

A robust relation between CWV and precipitation over land and ocean (seen here and in previous studies) provides a useful model constraint for the onset of deep convection. The GoAmazon2014/5 campaign (2014/15) near Manacapuru, Brazil, provides a unique opportunity to study how variability in moisture vertical structure and conditional instability of the environment control deep convective onset for smaller-scale and mesoscale convection alike, a difficult task in many regions because of observational constraints. Results shown previously for a tropical oceanic environment at the DOE ARM site at Nauru in the tropical western Pacific are examined as a basis for comparison.

There is little variability in moisture vertical structure across the seasonal and diurnal cycle at Nauru. The Amazon, however, has both a distinct seasonal and diurnal cycle in moisture vertical structure and associated variability. This makes the Amazon a good test case for examining variability in the moisture field and its effects on deep convection in the tropics. Mean moisture profiles show that the boundary layer at Nauru is moister than in the Amazon, while the lower free troposphere is drier. Moisture variance is large in the free troposphere at Nauru and the GoAmazon2014/5 site. The maximum (near 800 mb) is larger at Nauru than GoAmazon2014/5, and over land this maximum (~700 mb) is most evident in the drier months. During the wet season, moisture is less variable and more uniform throughout the column.

Over land, where larger diurnal and seasonal cycles exist, the onset of deep convection is strongly tied to lower-free-tropospheric moisture (700–900 mb) across all seasons and times of day, whereas the onset shows a strong relation to boundary layer moisture during the daytime only. The onset is characterized by the occurrence of locally occurring smaller-scale convection, as well as larger, mesoscale convective systems. During the daytime, smaller-scale convection is the most common convection type whereas mesoscale convective systems are a larger fraction of the total convection occurring during nighttime. The probability of mesoscale convection increases sharply with increasing lower-free-tropospheric humidity, whereas the relation to boundary layer moisture is less discernible. The probability of smaller-scale convection, however, is strongly tied to both lower-free-tropospheric moisture and boundary layer moisture. Smaller-scale convection occurs at lower values of lower-free-tropospheric humidity than mesoscale convection, most probably because of the strong influence of the boundary layer on isolated cells. The influence of the boundary layer is primarily confined to the daytime, whereas the lower-free-tropospheric moisture is strongly tied to both daytime and nocturnal convection.

Variability in lower-tropospheric humidity accounts for variability in the conditional instability of the environment, as estimated from buoyancy computations, and thus the onset of deep convection over both land and ocean, and across the seasonal and diurnal cycles to leading order. CWV is reaffirmed as a good proxy for conditional instability, yet since differences exist in the total moisture content of the lower troposphere for a given CWV regionally, seasonally, and diurnally, differences are thus observed in the observed onset of precipitation with CWV. For instance, more moisture in the daytime boundary layer and lower free troposphere for a given CWV allow for the onset of deep convection to occur at lower CWV in the dry-season daytime than wet-season daytime at the GoAmazon2014/5 site. Furthermore, the large range of environmental conditions across day and night and for the wet season and dry season at the GoAmazon2014/5 site permits inferences to be made about the relative success of different mixing assumptions as predictors of deep convective conditions. The criterion here is whether buoyancy computations based on a given mixing scheme (as summarized by an integrated buoyancy measure) can yield a strong relationship to the pickup in probability of precipitation. Given that the pickup can be seen as a function of layer-integrated water vapor, a buoyancy computation should yield at least as distinct a relationship to be considered successful. This comparison can be carried out separately for mesoscale and smaller-scale convection.

To examine the relation between observed deep convection and estimates of buoyancy, buoyancy was computed with four different assumptions of mixing between the plume and the environment using a simple mixing parameterization. A parcel buoyancy estimate with an assumption of deep-inflow mixing through a deep lower-tropospheric layer shows that a single formulation can capture the leading-order behavior controlling the onset of deep convection at both a tropical land and ocean site, across seasons and times of day, and

for both mesoscale and smaller-scale convection. Rather than suggesting an exact formulation for an optimal mixing profile, we provide evidence that even a simple mixing parameterization that appropriately weights boundary layer and lower-free-tropospheric air can be a useful predictor of deep convection across a range of scales.

Introducing deep-inflow mixing into a convective parameterization would not exclude the need for explicit treatments of organized convection (e.g., Mapes and Neale 2011; Khouider and Moncrieff 2015; Moncrieff et al. 2017), but it does suggest that a deep-inflow framework for mixing in the buoyancy calculations could be useful even in presence of organization. While other factors would have to determine the parameterization of organization, the indications are that a consistent mixing framework with deep-inflow characteristics could work for both organized and unorganized convection. We interpret this as the organized convection being sustained by the same basic mechanisms driving buoyancy, with the inflow of environmental air into updrafts coming from a roughly similar deep layer in both cases. Even when the mesoscale systems are preexisting and propagating into the region where the sounding is observed, lack of conditional instability (given suitable inflow assumptions) yields low probability of that system continuing to produce precipitation.

The results here suggest implementing deep-inflow mixing in a convective parameterization might be helpful in reducing long-standing precipitation biases in regions like the Amazon. Though we present evidence here and in Schiro et al. (2018) of deep-inflow mixing by analyzing statistical properties of deep convection, we do not suggest that the deep-inflow framework is universal; instead, we suggest that it is generally consistent with the dependence of convective onset on lower-free-tropospheric moisture and with estimates of mass flux. We further underline that the statistics presented here emphasize strongly precipitating systems, so the measures of success of deep-inflow mixing apply only to convection contributing substantially to precipitation. Future field campaigns and satellite missions capable of capturing spatiotemporal variability of moisture and precipitation at sufficiently high resolution could more effectively test these hypotheses and greatly improve our understanding of the relation between moisture, instability, and deep convective onset across scales.

Acknowledgments. The U.S. Department of Energy Atmospheric Radiation Measurement (ARM) Climate Research Facility GoAmazon2014/5 and tropical west Pacific field campaign data were essential to this work. This research was supported in part by the Office of Biological and Environmental Research of the U.S. Department of Energy Grant DE-SC0011074, National Science Foundation Grant AGS-1505198, National Oceanic and Atmospheric Administration Grant NA14OAR4310274, and a Dissertation Year from the University of California, Los Angeles, Fellowship (KS). Parts of this material have been presented at the fall 2016 and fall 2017 meetings of the American Geophysical Union and have formed part of K. Schiro's Ph.D. thesis.

REFERENCES

Adams, D. K., S. I. Gutman, K. L. Holub, and D. S. Pereira, 2013: GNSS observations of deep convective time scales in the Amazon. *Geophys. Res. Lett.*, **40**, 2818–2823, https://doi.org/10.1002/grl.50573.

Ahmed, F., and C. Schumacher, 2015: Convective and stratiform components of the precipitation-moisture relationship. *Geophys. Res. Lett.*, **10**, 453–462, https://doi.org/10.1002/2015GL066957.

——, and ——, 2017: Geographical differences in the tropical precipitation-moisture relationship and rain intensity onset. *Geophys. Res. Lett.*, **44**, 1114–1122, https://doi.org/10.1002/2016GL071980.

——, and J. D. Neelin, 2018: Reverse engineering the tropical precipitation–buoyancy relationship. *J. Atmos. Sci.*, **75**, 1587–1608, https://doi.org/10.1175/JAS-D-17-0333.1.

Anderson, N. F., C. A. Grainger, and J. L. Stith, 2005: Characteristics of strong updrafts in precipitating systems over the central tropical Pacific Ocean and in the Amazon. *J. Appl. Meteor.*, **44**, 731–738, https://doi.org/10.1175/JAM2231.1.

Andreae, M. O., D. Rosenfeld, P. Artaxo, A. A. Costa, G. P. Frank, K. M. Longo, and M. A. F. Silva-Dias, 2004: Smoking rain clouds over the Amazon. *Science*, **303**, 1337–1342, https://doi.org/10.1126/science.1092779.

ARM Climate Research Facility, 2013a: MWR retrievals (MWRRET1LILJCLOU). ARM Climate Research Facility Data Archive. Subset used: 10 January 2014–20 October 2015, https://doi.org/10.5439/1027369.

——, 2013b: Radiosonde retrievals (SONDE). ARM Climate Research Facility Data Archive. Subset used: 10 January 2014–20 October 2015, https://doi.org/10.5439/1021460.

——, 2013c: AOSMET precipitation (AOSMET). ARM Climate Research Facility Data Archive. Subset used: 10 January 2014–20 October 2015, https://doi.org/10.5439/1025153.

——, 2014a: W-band cloud radar active remote sensing of cloud (ARSCLWACR1KOLLIAS). ARM Climate Research Facility Data Archive. Subset used: 18 February 2014–20 October 2015, https://doi.org/10.5439/1097547.

——, 2014b: W-band cloud radar active remote sensing of cloud (ARSCLWACRBND1KOLLIAS). ARM Climate Research Facility Data Archive. Subset used: 18 February 2014–20 October 2015, https://doi.org/10.5439/1097548.

Bechtold, P., J. P. Chaboureau, A. Beljaars, A. K. Betts, M. Köhler, M. Miller, and J. L. Redelsperger, 2004: The simulation of the diurnal cycle of convective precipitation over land in a global model. *Quart. J. Roy. Meteor. Soc.*, **130**, 3119–3137, https://doi.org/10.1256/qj.03.103.

Bernstein, D. N., and J. D. Neelin, 2016: Identifying sensitive ranges in global warming precipitation change dependence on convective parameters. *Geophys. Res. Lett.*, **43**, 5841–5850, https://doi.org/10.1002/2016GL069022.

Betts, A. K., and C. Jakob, 2002: Study of diurnal cycle of convective precipitation over Amazonia using a single column model. *J. Geophys. Res.*, **107**, 4732, https://doi.org/10.1029/2002JD002264.

Böing, S. J., H. J. Jonker, A. P. Siebesma, and W. W. Grabowski, 2012: Influence of the subcloud layer on the development of a deep convective ensemble. *J. Atmos. Sci.*, **69**, 2682–2698, https://doi.org/10.1175/JAS-D-11-0317.1.

Bretherton, C. S., M. E. Peters, and L. E. Back, 2004: Relationships between water vapor path and precipitation over the tropical oceans. *J. Climate*, **17**, 1517–1528, https://doi.org/10.1175/1520-0442(2004)017<1517:RBWVPA>2.0.CO;2.

Brown, R. G., and C. Zhang, 1997: Variability of midtropospheric moisture and its effect on cloud-top height distribution during TOGA COARE. *J. Atmos. Sci.*, **54**, 2760–2774, https://doi.org/10.1175/1520-0469(1997)054<2760:VOMMAI>2.0.CO;2.

Chaboureau, J. P., F. Guichard, J. L. Redelsperger, and J. P. Lafore, 2004: The role of stability and moisture in the diurnal cycle of convection over land. *Quart. J. Roy. Meteor. Soc.*, **130**, 3105–3117, https://doi.org/10.1256/qj.03.132.

Churchill, D. D., and R. A. Houze Jr., 1984: Development and structure of winter monsoon cloud clusters on 10 December 1978. *J. Atmos. Sci.*, **41**, 933–960, https://doi.org/10.1175/1520-0469(1984)041<0933:DASOWM>2.0.CO;2.

D'Andrea, F., P. Gentine, A. K. Betts, and B. R. Lintner, 2014: Triggering deep convection with a probabilistic plume model. *J. Atmos. Sci.*, **71**, 3881–3901, https://doi.org/10.1175/JAS-D-13-0340.1.

Del Genio, A. D., 2012: Representing the sensitivity of convective cloud systems to tropospheric humidity in general circulation models. *Surv. Geophys.*, **33**, 637–656, https://doi.org/10.1007/s10712-011-9148-9.

——, and J. Wu, 2010: The role of entrainment in the diurnal cycle of continental convection. *J. Climate*, **23**, 2722–2738, https://doi.org/10.1175/2009JCLI3340.1.

——, Y. H. Chen, D. Kim, and M. S. Yao, 2012: The MJO transition from shallow to deep convection in *CloudSat/CALIPSO* data and GISS GCM simulations. *J. Climate*, **25**, 3755–3770, https://doi.org/10.1175/JCLI-D-11-00384.1.

Derbyshire, S. H., I. Beau, P. Bechtold, J.-Y. Gandpeix, J.-M. Piriou, J.-L. Redelsperger, and P. Soares, 2004: Sensitivity of moist convection to environmental humidity. *Quart. J. Roy. Meteor. Soc.*, **130**, 3055–3079, https://doi.org/10.1256/qj.03.130.

Giangrande, S. E., and Coauthors, 2016: Convective cloud vertical velocity and mass-flux characteristics from radar wind profiler observations during GoAmazon2014/5. *J. Geophys. Res. Atmos.*, **121**, 12 891–12 913, https://doi.org/10.1002/2016JD025303.

Gonzalez, A. O., and X. Jiang, 2017: Winter mean lower tropospheric moisture over the Maritime Continent as a climate model diagnostic metric for the propagation of the Madden-Julian oscillation. *Geophys. Res. Lett.*, **44**, 2588–2596, https://doi.org/10.1002/2016GL072430.

Grabowski, W. W., and H. Morrison, 2017: Modeling condensation in deep convection. *J. Atmos. Sci.*, **74**, 2247–2267, https://doi.org/10.1175/JAS-D-16-0255.1.

Guichard, F., and Coauthors, 2004: Modelling the diurnal cycle of deep precipitating convection over land with cloud-resolving models and single-column models. *Quart. J. Roy. Meteor. Soc.*, **130**, 3139–3172, https://doi.org/10.1256/qj.03.145.

Hannah, W. M., and E. D. Maloney, 2011: The role of moisture–convection feedbacks in simulating the Madden–Julian oscillation. *J. Climate*, **24**, 2754–2770, https://doi.org/10.1175/2011JCLI3803.1.

Hernandez-Deckers, D., and S. C. Sherwood, 2018: On the role of entrainment in the fate of cumulus thermals. *J. Atmos. Sci.*, **75**, 3911–3924, https://doi.org/10.1175/JAS-D-18-0077.1.

Hohenegger, C., and B. Stevens, 2013: Preconditioning deep convection with cumulus congestus. *J. Atmos. Sci.*, **70**, 448–464, https://doi.org/10.1175/JAS-D-12-089.1.

Holdridge, D., J. Kyrouac, and R. Coulter, 2013: Balloon-borne sounding system (SONDEWNPN). ARM Climate Research Facility Data Archive. Subset used: 10 January 2014–20 October 2015, https://doi.org/10.5439/1021460.

Holloway, C. E., and J. D. Neelin, 2009: Moisture vertical structure, column water vapor, and tropical deep convection. *J. Atmos. Sci.*, **66**, 1665–1683, https://doi.org/10.1175/2008JAS2806.1.

——, and ——, 2010: Temporal relations of column water vapor and tropical precipitation. *J. Atmos. Sci.*, **67**, 1091–1105, https://doi.org/10.1175/2009JAS3284.1.

Houze, R. A., Jr., 2004: Mesoscale convective systems. *Rev. Geophys.*, **42**, RG4003, https://doi.org/10.1029/2004RG000150.

Khairoutdinov, M., and D. Randall, 2006: High-resolution simulation of shallow-to-deep convection transition over land. *J. Atmos. Sci.*, **63**, 3421–3436, https://doi.org/10.1175/JAS3810.1.

Khouider, B., and M. W. Moncrieff, 2015: Organized convection parameterization for the ITCZ. *J. Atmos. Sci.*, **72**, 3073–3096, https://doi.org/10.1175/JAS-D-15-0006.1.

Kim, D., and Coauthors, 2014: Process-oriented MJO simulation diagnostic: Moisture sensitivity of simulated convection. *J. Climate*, **27**, 5379–5395, https://doi.org/10.1175/JCLI-D-13-00497.1.

Kingsmill, D. E., and R. A. Houze Jr., 1999: Kinematic characteristics of air flowing into and out of precipitating convection over the west Pacific warm pool: An airborne Doppler radar survey. *Quart. J. Roy. Meteor. Soc.*, **125**, 1165–1207, https://doi.org/10.1002/qj.1999.49712555605.

Klocke, D., R. Pincus, and J. Quaas, 2011: On constraining estimates of climate sensitivity with present-day observations through model weighting. *J. Climate*, **24**, 6092–6099, https://doi.org/10.1175/2011JCLI4193.1.

Knievel, J. C., D. A. Ahijevych, and K. W. Manning, 2004: Using temporal modes of rainfall to evaluate the performance of a numerical weather prediction model. *Mon. Wea. Rev.*, **132**, 2995–3009, https://doi.org/10.1175/MWR2828.1.

Knight, C. G., and Coauthors, 2007: Association of parameter, software, and hardware variation with large-scale behavior across 57,000 climate models. *Proc. Natl. Acad. Sci. USA*, **104**, 12 259–12 264, https://doi.org/10.1073/pnas.0608144104.

Kumar, V. V., C. Jakob, A. Protat, P. T. May, and L. Davies, 2013: The four cumulus cloud modes and their progression during rainfall events: AC-band polarimetric radar perspective. *J. Geophys. Res. Atmos.*, **118**, 8375–8389, https://doi.org/10.1002/jgrd.50640.

——, ——, ——, C. R. Williams, and P. T. May, 2015: Mass-flux characteristics of tropical cumulus clouds from wind profiler observations at Darwin, Australia. *J. Atmos. Sci.*, **72**, 1837–1855, https://doi.org/10.1175/JAS-D-14-0259.1.

——, A. Protat, C. Jakob, C. R. Williams, S. Rauniyar, G. L. Stephens, and P. T. May, 2016: The estimation of convective mass flux from radar reflectivities. *J. Appl. Meteor. Climatol.*, **55**, 1239–1257, https://doi.org/10.1175/JAMC-D-15-0193.1.

Kuo, Y.-H., J. D. Neelin, and C. R. Mechoso, 2017: Tropical convective transition statistics and causality in the water vapor–precipitation relation. *J. Atmos. Sci.*, **74**, 915–931, https://doi.org/10.1175/JAS-D-16-0182.1.

——, K. A. Schiro, and J. D. Neelin, 2018: Convective transition statistics over tropical oceans for climate model diagnostics:

Observational baseline. *J. Atmos. Sci.*, **75**, 1553–1570, https://doi.org/10.1175/JAS-D-17-0287.1.

Kurowski, M. J., K. Suselj, W. W. Grabowski, and J. Teixeira, 2018: Shallow-to-deep transition of continental moist convection: Cold pools, surface fluxes, and mesoscale organization. *J. Atmos. Sci.*, **75**, 4071–4090, https://doi.org/10.1175/JAS-D-18-0031.1.

Lee, M. I., and Coauthors, 2007: Sensitivity to horizontal resolution in the AGCM simulations of warm season diurnal cycle of precipitation over the United States and northern Mexico. *J. Climate*, **20**, 1862–1881, https://doi.org/10.1175/JCLI4090.1.

LeMone, M. A., and E. J. Zipser, 1980: Cumulonimbus vertical velocity events in GATE. Part I: Diameter, intensity and mass flux. *J. Atmos. Sci.*, **37**, 2444–2457, https://doi.org/10.1175/1520-0469(1980)037<2444:CVVEIG>2.0.CO;2.

Liang, X.-Z., L. Li, A. Dai, and K. E. Kunkel, 2004: Regional climate model simulation of summer precipitation diurnal cycle over the United States. *Geophys. Res. Lett.*, **31**, L24208, https://doi.org/10.1029/2004GL021054.

Lintner, B. R., D. K. Adams, K. A. Schiro, A. M. Stansfield, A. da Rocha, and J. D. Neelin, 2017: Relationships among climatological moisture vertical structure, column water vapor, and precipitation over the central Amazon in CMIP5 models. *Geophys. Res. Lett.*, **44**, 1981–1989, https://doi.org/10.1002/2016GL071923.

Lucas, C., E. J. Zipser, and M. A. LeMone, 1994: Vertical velocity in oceanic convection off tropical Australia. *J. Atmos. Sci.*, **51**, 3183–3193, https://doi.org/10.1175/1520-0469(1994)051<3183:VVIOCO>2.0.CO;2.

Machado, L. A. T., H. Laurent, N. Dessay, and I. Miranda, 2004: Seasonal and diurnal variability of convection over the Amazonia: A comparison of different vegetation types and large scale forcing. *Theor. Appl. Climatol.*, **78**, 61–77, https://doi.org/10.1007/s00704-004-0044-9.

Mapes, B., and R. Neale, 2011: Parameterizing convective organization to escape the entrainment dilemma. *J. Adv. Model. Earth Syst.*, **3**, M06004, https://doi.org/10.1029/2011MS000042.

Martin, S. T., and Coauthors, 2016: Introduction: Observations and modeling of the Green Ocean Amazon (GoAmazon2014/5). *Atmos. Chem. Phys.*, **16**, 4785–4796, https://doi.org/10.5194/acp-16-4785-2016.

Masunaga, H., and Z. J. Luo, 2016: Convective and large-scale mass flux profiles over tropical oceans determined from synergistic analysis of a suite of satellite observations. *J. Geophys. Res. Atmos.*, **121**, 7958–7974, https://doi.org/10.1002/2016JD024753.

McGee, C. J., and S. C. van den Heever, 2014: Latent heating and mixing due to entrainment in tropical deep convection. *J. Atmos. Sci.*, **71**, 816–832, https://doi.org/10.1175/JAS-D-13-0140.1.

Mechem, D. B., R. A. Houze Jr., and S. S. Chen, 2002: Layer inflow into precipitating convection over the western tropical Pacific. *Quart. J. Roy. Meteor. Soc.*, **128**, 1997–2030, https://doi.org/10.1256/003590002320603502.

Mishra, S. K., and J. Srinivasan, 2010: Sensitivity of the simulated precipitation to changes in convective relaxation time scale. *Ann. Geophys.*, **28**, 1827–1846, https://doi.org/10.5194/angeo-28-1827-2010.

Moncrieff, M. W., C. Liu, and P. Bogenschutz, 2017: Simulation, modeling, and dynamically based parameterization of organized tropical convection for global climate models. *J. Atmos. Sci.*, **74**, 1363–1380, https://doi.org/10.1175/JAS-D-16-0166.1.

Mrowiec, A. A., C. Rio, A. M. Fridlind, A. S. Ackerman, A. D. Del Genio, O. M. Pauluis, A. C. Varble, and J. Fan, 2012: Analysis of cloud-resolving simulations of a tropical mesoscale convective system observed during TWP-ICE: Vertical fluxes and draft properties in convective and stratiform regions. *J. Geophys. Res.*, **117**, D19201, https://doi.org/10.1029/2012JD017759.

Muller, C. J., L. E. Back, P. A. O'Gorman, and K. A. Emanuel, 2009: A model for the relationship between tropical precipitation and column water vapor. *Geophys. Res. Lett.*, **36**, L16804, https://doi.org/10.1029/2009GL039667.

Murphy, J. M., D. M. H. Sexton, D. N. Barnett, G. S. Jones, M. J. Webb, M. Collins, and D. A. Stainforth, 2004: Quantification of modelling uncertainties in a large ensemble of climate change simulations. *Nature*, **430**, 768–772, https://doi.org/10.1038/nature02771.

Neelin, J. D., O. Peters, and K. Hales, 2009: The transition to strong convection. *J. Atmos. Sci.*, **66**, 2367–2384, https://doi.org/10.1175/2009JAS2962.1.

Neggers, R. A. J., A. P. Siebesma, and H. J. J. Jonker, 2002: A multiparcel model for shallow cumulus convection. *J. Atmos. Sci.*, **59**, 1655–1668, https://doi.org/10.1175/1520-0469(2002)059<1655:AMMFSC>2.0.CO;2.

Nesbitt, S. W., and E. J. Zipser, 2003: The diurnal cycle of rainfall and convective intensity according to three years of TRMM measurements. *J. Climate*, **16**, 1456–1475, https://doi.org/10.1175/1520-0442-16.10.1456.

——, R. Cifelli, and S. A. Rutledge, 2006: Storm morphology and rainfall characteristics of TRMM precipitation features. *Mon. Wea. Rev.*, **134**, 2702–2721, https://doi.org/10.1175/MWR3200.1.

Oueslati, B., and G. Bellon, 2013: Convective entrainment and large-scale organization of tropical precipitation: Sensitivity of the CNRM-CM5 hierarchy of models. *J. Climate*, **26**, 2931–2946, https://doi.org/10.1175/JCLI-D-12-00314.1.

Peters, O., and J. D. Neelin, 2006: Critical phenomena in atmospheric precipitation. *Nat. Phys.*, **2**, 393–396, https://doi.org/10.1038/nphys314.

Raymond, D. J., 2000: Thermodynamic control of tropical rainfall. *Quart. J. Roy. Meteor. Soc.*, **126**, 889–898, https://doi.org/10.1002/qj.49712656406.

——, and A. M. Blyth, 1986: A stochastic mixing model for nonprecipitating cumulus clouds. *J. Atmos. Sci.*, **43**, 2708–2718, https://doi.org/10.1175/1520-0469(1986)043<2708:ASMMFN>2.0.CO;2.

Robe, F. R., and K. A. Emanuel, 1996: Moist convective scaling: Some inferences from three-dimensional cloud ensemble simulations. *J. Atmos. Sci.*, **53**, 3265–3275, https://doi.org/10.1175/1520-0469(1996)053<3265:MCSSIF>2.0.CO;2.

Romps, D. M., 2010: A direct measure of entrainment. *J. Atmos. Sci.*, **67**, 1908–1927, https://doi.org/10.1175/2010JAS3371.1.

——, and Z. Kuang, 2010: Nature versus nurture in shallow convection. *J. Atmos. Sci.*, **67**, 1655–1666, https://doi.org/10.1175/2009JAS3307.1.

Rosenfeld, D., U. Lohmann, G. B. Raga, C. D. O'Dowd, M. Kulmala, S. Fuzzi, A. Reissell, and M. Andreae, 2008: Flood or drought: How do aerosols affect precipitation? *Science*, **321**, 1309–1313, https://doi.org/10.1126/science.1160606.

Rotunno, R., J. B. Klemp, and M. L. Weisman, 1988: A theory for strong, long-lived squall lines. *J. Atmos. Sci.*, **45**, 463–485, https://doi.org/10.1175/1520-0469(1988)045<0463:ATFSLL>2.0.CO;2.

Sahany, S., J. D. Neelin, K. Hales, and R. B. Neale, 2012: Temperature–moisture dependence of the deep convective transition as a constraint on entrainment in climate models. *J. Atmos. Sci.*, **69**, 1340–1358, https://doi.org/10.1175/JAS-D-11-0164.1.

Sanderson, B. M., and Coauthors, 2008: Constraints on model response to greenhouse gas forcing and the role of subgrid-scale

processes. *J. Climate*, **21**, 2384–2400, https://doi.org/10.1175/2008JCLI1869.1.

Schiro, K. A., J. D. Neelin, D. K. Adams, and B. R. Lintner, 2016: Deep convection and column water vapor over tropical land versus tropical ocean: A comparison between the Amazon and the tropical western Pacific. *J. Atmos. Sci.*, **73**, 4043–4063, https://doi.org/10.1175/JAS-D-16-0119.1.

——, F. Ahmed, S. E. Giangrande, and J. D. Neelin, 2018: GoAmazon2014/5 points to deep-inflow approach to mesoscale-organized and unorganized deep convection. *Proc. Natl. Acad. Sci. USA*, **115**, 4577–4582, https://doi.org/10.1073/pnas.1719842115.

Schlemmer, L., and C. Hohenegger, 2014: The formation of wider and deeper clouds as a result of cold-pool dynamics. *J. Atmos. Sci.*, **71**, 2842–2858, https://doi.org/10.1175/JAS-D-13-0170.1.

Schumacher, C., 2015: Observations and modeling of the Green Ocean Amazon (GOAMAZON), SIPAM Manaus S-band radar. ARM Climate Research Facility Data Archive. Subset used: 10 January 2014–20 October 2015, accessed 8 February 2018, https://www.arm.gov/.

Siebesma, A. P., and Coauthors, 2003: A large eddy simulation intercomparison study of shallow cumulus convection. *J. Atmos. Sci.*, **60**, 1201–1219, https://doi.org/10.1175/1520-0469(2003)60<1201:ALESIS>2.0.CO;2.

——, P. M. M. Soares, and J. Teixeira, 2007: A combined eddy-diffusivity mass-flux approach for the convective boundary layer. *J. Atmos. Sci.*, **64**, 1230–1248, https://doi.org/10.1175/JAS3888.1.

Simpson, J., and V. Wiggert, 1969: Models of precipitating cumulus towers. *Mon. Wea. Rev.*, **97**, 471–489, https://doi.org/10.1175/1520-0493(1969)097<0471:MOPCT>2.3.CO;2.

Soares, P. M. M., P. M. A. Miranda, A. P. Siebesma, and J. Teixeira, 2004: An eddy-diffusivity/mass-flux parameterization for dry and shallow cumulus convection. *Quart. J. Roy. Meteor. Soc.*, **130**, 3365–3383, https://doi.org/10.1256/qj.03.223.

Sobel, A. H., and G. Bellon, 2009: The effect of imposed drying on parameterized deep convection. *J. Atmos. Sci.*, **66**, 2085–2096, https://doi.org/10.1175/2008JAS2926.1.

——, S. E. Yuter, C. S. Bretherton, and G. N. Kiladis, 2004: Large-scale meteorology and deep convection during TRMM KWAJEX. *Mon. Wea. Rev.*, **132**, 422–444, https://doi.org/10.1175/1520-0493(2004)132<0422:LMADCD>2.0.CO;2.

Stechmann, S. N., and J. D. Neelin, 2011: A stochastic model for the transition to strong convection. *J. Atmos. Sci.*, **68**, 2955–2970, https://doi.org/10.1175/JAS-D-11-028.1.

——, and ——, 2014: First-passage-time prototypes for precipitation statistics. *J. Atmos. Sci.*, **71**, 3269–3291, https://doi.org/10.1175/JAS-D-13-0268.1.

Steiner, M., R. A. Houze Jr., and S. E. Yuter, 1995: Climatological characterization of three-dimensional storm structure from operational radar and rain gauge data. *J. Appl. Meteor.*, **34**, 1978–2007, https://doi.org/10.1175/1520-0450(1995)034<1978:CCOTDS>2.0.CO;2.

Suhas, E., and G. J. Zhang, 2014: Evaluation of trigger functions for convective parameterization schemes using observations. *J. Climate*, **27**, 7647–7666, https://doi.org/10.1175/JCLI-D-13-00718.1.

Suselj, K., T. F. Hogan, and J. Teixeira, 2014: Implementation of a stochastic eddy-diffusivity/mass-flux parameterization into the Navy Global Environmental Model. *Wea. Forecasting*, **29**, 1374–1390, https://doi.org/10.1175/WAF-D-14-00043.1.

Tompkins, A. M., 2001: Organization of tropical convection in low vertical wind shears: The role of cold pools. *J. Atmos. Sci.*, **58**, 1650–1672, https://doi.org/10.1175/1520-0469(2001)058<1650:OOTCIL>2.0.CO;2.

Turner, D. D., S. A. Clough, J. C. Liljegren, E. E. Clothiaux, K. E. Cady-Pereira, and K. L. Gaustad, 2007: Retrieving liquid water path and precipitable water vapor from the Atmospheric Radiation Measurement (ARM) microwave radiometers. *IEEE Trans. Geosci. Remote Sens.*, **45**, 3680–3690, https://doi.org/10.1109/TGRS.2007.903703.

Vila, D. A., L. Machado, H. Laurent, and I. Velasco, 2008: Forecast and Tracking the Evolution of Cloud Clusters (ForTraCC) using satellite infrared imagery: Methodology and validation. *Wea. Forecasting*, **23**, 233–245, https://doi.org/10.1175/2007WAF2006121.1.

Wang, W., and X. Liu, 2009: Evaluating deep updraft formulation in NCAR CAM3 with high-resolution WRF simulations during ARM TWP-ICE. *Geophys. Res. Lett.*, **36**, L04701, https://doi.org/10.1029/2008GL036692.

Xie, S., M. Zhang, J. S. Boyle, R. T. Cederwall, G. L. Potter, and W. Lin, 2004: Impact of a revised convective triggering mechanism on Community Atmosphere Model, version 2, simulations: Results from short-range weather forecasts. *J. Geophys. Res.*, **109**, D14102, https://doi.org/10.1029/2004JD004692.

Yang, J., Z. Wang, A. J. Heymsfield, and J. R. French, 2016: Characteristics of vertical air motion in isolated convective clouds. *Atmos. Chem. Phys.*, **16**, 10 159–10 173, https://doi.org/10.5194/acp-16-10159-2016.

Yeo, K., and D. M. Romps, 2013: Measurement of convective entrainment using Lagrangian particles. *J. Atmos. Sci.*, **70**, 266–277, https://doi.org/10.1175/JAS-D-12-0144.1.

Zhang, Y., and S. A. Klein, 2010: Mechanisms affecting the transition from shallow to deep convection over land: Inferences from observations of the diurnal cycle collected at the ARM Southern Great Plains site. *J. Atmos. Sci.*, **67**, 2943–2959, https://doi.org/10.1175/2010JAS3366.1.

Zhu, P., 2015: On the mass-flux representation of vertical transport in moist convection. *J. Atmos. Sci.*, **72**, 4445–4468, https://doi.org/10.1175/JAS-D-14-0332.1.

Zhuang, Y., R. Fu, and H. Wang, 2018: How do environmental conditions influence vertical buoyancy structure and shallow-to-deep convection transition across different climate regimes? *J. Atmos. Sci.*, **75**, 1909–1932, https://doi.org/10.1175/JAS-D-17-0284.1.